AN OPTIMIZATION APPROACH TO WHITE MATTER BRAIN TUMOR RESECTION

A THESIS SUBMITTED TO
THE GRADUATE SCHOOL OF ENGINEERING AND SCIENCE
OF BILKENT UNIVERSITY
IN PARTIAL FULFILLMENT OF THE REQUIREMENTS FOR
THE DEGREE OF
MASTER OF SCIENCE
IN
INDUSTRIAL ENGINEERING

By
Sena Aslı Bozkurt
July 2025

AN OPTIMIZATION APPROACH TO WHITE MATTER BRAIN TUMOR RESECTION

By Sena Aslı Bozkurt

July 2025

We certify that we have read this thesis and that in our opinion it is fully adequate, in scope and in quality, as a thesis for the degree of Master of Science.

Oya Karaşan(Advisor)

Taghi Khaniyev(Co-Advisor)

Oleg Prokopyev

Bahar Yetiş

Approved for the Graduate School of Engineering and Science:

Orhan Arıkan
Director of the Graduate School

ABSTRACT

AN OPTIMIZATION APPROACH TO WHITE MATTER BRAIN TUMOR RESECTION

Sena Aslı Bozkurt
M.S. in Industrial Engineering
Advisor: Oya Karaşan
Co-Advisor: Taghi Khaniyev
July 2025

Preserving brain functionality while performing maximal tumor resection remains a significant challenge in current clinical practice, as existing approaches do not offer a systematic framework to balance tumor removal with functional outcomes. To address this, we developed a mathematical optimization model for brain tumor resection problem that aims to preserve network efficiency as much as possible by resecting a predefined volume of tumor. Network efficiency is quantified using the Global Efficiency (GE) metric. The model includes spatial contiguity constraints to ensure that the resected area forms a clinically realistic connected region. To improve computational efficiency and scalability, we proposed enhanced formulations and introduced an aggregation heuristic that groups nodes that are physically closer to each other, significantly reducing solution time while maintaining high-quality results. For the experimental analysis, we used real brain network data representing healthy white and gray matter regions and generated synthetic tumor instances and modeled their disruptive impact on the brain network. We first validated the performance of the aggregation heuristic by comparing it against the original model. Results show that the heuristic drastically reduces computational time while achieving comparable GE values. We then investigated the impact of tumor size and found that larger tumors disrupt the network more severely even before resection, and lead to lower GE values post-resection at the same threshold levels. Then, we examined the impact of tumor location and observed that centrally located tumors lead to greater decreases in GE compared to peripheral tumors when the same tumor volume is removed. Finally, using a real tumor instance, we compared the "best" resection guided by our model with the "worst" resection, and demonstrated that our approach leads to significantly better preservation of brain network efficiency.

Keywords: Brain Tumor Resection, Global Efficiency, Network Modeling, Mathematical Optimization, Contiguity Constraints, Aggregation Heuristic.

ÖZET

BEYAZ CEVHERDE KONUMLANMIŞ BEYİN TÜMÖR ÇIKARIMINA OPTİMİZASYON YAKLAŞIMI

Sena Aslı Bozkurt
Endüstri Mühendisliği, Yüksek Lisans
Tez Danışmanı: Oya Karaşan
İkinci Tez Danışmanı: Taghi Khaniyev
Temmuz 2025

Mevcut klinik uygulamalarda beyin tümörlerin maksimum düzeyde çıkarılması hedeflenmektedir; ancak bu süreçte beyin fonksiyonlarının korunması sistematik bir yaklaşıma dayanmamaktadır. Bu problemi ele almak amacıyla, belirli bir eşik değerin üzerindeki tümörlü bölgeleri çıkarırken beyin ağının işlevselliğini maksimize etmeyi hedefleyen matematiksel bir optimizasyon modeli geliştirdik. Ağ işlevselliği, Global Efficiency (GE) metriği kullanılarak nicelenmiştir. Model, çıkarılan alanın klinik açıdan gerçekşi bir şekilde bağlı bir bölge oluşturmasını sağlamak amacıyla Komşuluk kısıtlarını içermektedir. Modelin hesaplama verimliliğini artırmak için, benzer özelliklere sahip düğümlerin toplulaştırıldığı (aggregation) bir sezgisel yöntem tanıttık. Gerçek sağlıklı gri ve beyaz madde ağı verisini kullanarak sentetik tümör örnekleri oluşturduk ve bu tümörlerin beyin ağını bozucu etkisini optimizasyon modeliyle belirledik. Toplulaştırma sezgisinin orijinal modele benzer sonuçlar verirken hesaplama süresini büyük ölçüde azalttığını gösterdik. Tümör boyutu arttıkça, henüz hiç bölge çıkarılmadan dahi beyin ağında daha fazla bozulma meydana geldiğini ve aynı eşiklerde daha düşük global verimlilik değerleri gözlendiğini belirledik. Ayrıca, tümör konumu analizlerinde, beynin merkezine yerleşmiş tümörlerin, aynı hacim çıkarıldığında dış bölgedeki tümörlere göre daha fazla global verimlilik azalmasına yol açtığını gösterdik. Son olarak, Hacettepe Üniversitesi'nde elde edilen gerçek bir tümör örneği üzerinde modelimizi test ettik. En iyi olasılıkla planlanan rezeksiyon ile en kötü senaryo arasında karşılaştırmalar yapıldı ve modelimizin beyin ağı verimliliğini anlamlı bir farkla daha iyi koruduğu gösterildi.

Anahtar sözcükler: Beyin Tümör Rezeksiyonu, Küresel Verimlilik, Ağ Modelleme, Matematiksel Optimizasyon, Komşuluk Kısıtlamaları, Toplulaştırma Sezgisi .

Acknowledgement

First and foremost, I would like to express my deepest gratitude to my supervisors, Prof. Oya Karaşan and Asst. Prof. Taghi Khaniyev, for their invaluable guidance, support, and encouragement throughout this journey. Their insightful feedback, patience, and expertise have been instrumental in shaping this thesis and my development as a researcher.

I am sincerely thankful to the members of my thesis defense jury, Prof. Bahar Yetiş and Prof. Oleg Prokopyev, for their time, thoughtful questions, and constructive feedback, which helped improve the quality of this work.

I would like to acknowledge the financial support of The Scientific and Technological Research Council of Turkey (TUBITAK) for the 2210-A National Graduate Study Scholarship Program they awarded.

I am deeply grateful to my family—my mother Özden Bozkurt, my father Halit Bozkurt, my brother Oğuz Bozkurt and my cousin Esra Zeynep Şenel—for their unwavering love and support. Their belief in me has been a constant source of strength. A special thanks to my aunt, Gülcan Şenel, for her encouragement and for always being there during the most challenging times.

To my dear friends—Ali Bingöl, Bora Çetin, Doğancan Koyuncu, Elanur Çöplü, Fatmagül Ezgi Kabak, İpek Mocul, Mustafa Günal, Özge Yaren Akın, Umut Ceyda Serhat, Yalın Mocan, and Yiğit Ateş—thank you for the laughter, late-night conversations, and kind words when I needed them most. I am especially thankful to Kaan Çakıroğlu, for his patience, understanding, and for making this journey all the more enjoyable.

I am also grateful to my fellow graduate students and colleagues—Doğuş Berk Koçak, Deniz Akkaya, Osman Kağan Yayla, Muhittin Can Korkut, Efecan Şentürk, Zeynep Şahin, Şebnem Kılıç, and Defne Tan—for sharing in both the challenges and triumphs of graduate life. I would also like to thank Elif Rana Yöner for her companionship and support throughout my studies.

This thesis would not have been possible without the support of each and every one of you.

Contents

List of Figures

List of Tables

Chapter 1

Introduction

Brain tumors are formed due to abnormal growth of brain cells or their surrounding tissues. They range from primary tumors that originate in the brain to secondary tumors that spread from other parts of the body. Whether primary or secondary, they present a complex challenge due to their varying behaviors, from slow-growing benign masses to aggressive malignancies. Low-grade glioma (LGG), a primary tumor, is a type of tumor arising from glial cells, which supports and protects the brain cells of the central nervous system [3]. A sub-type of LGG, diffuse low-grade glioma is a rare neurological tumor characterized by slow but continuous progress and tumor recurrences. It is generally revealed by seizures in young adults with no or only mild neurological deficits [4]. On the other hand, their slow progression allows the brain to gradually compensate for damaged areas [5]. As their incidences increase, there is a growing need for advancements in diagnosis and treatment. A real LGG instance located in the white matter is shown in Figure 1.1. The red circle outlines the tumorous area.

Currently, the standard practice for brain tumor treatment includes surgical resection followed by radiotherapy, and chemotherapy. Radiotherapy benefits patients with the highest probability of tumor growth the most, although its effect on overall survival is minimal; consequently, it is typically offered to higher-risk patients and those who experience tumor growth progression after chemotherapy

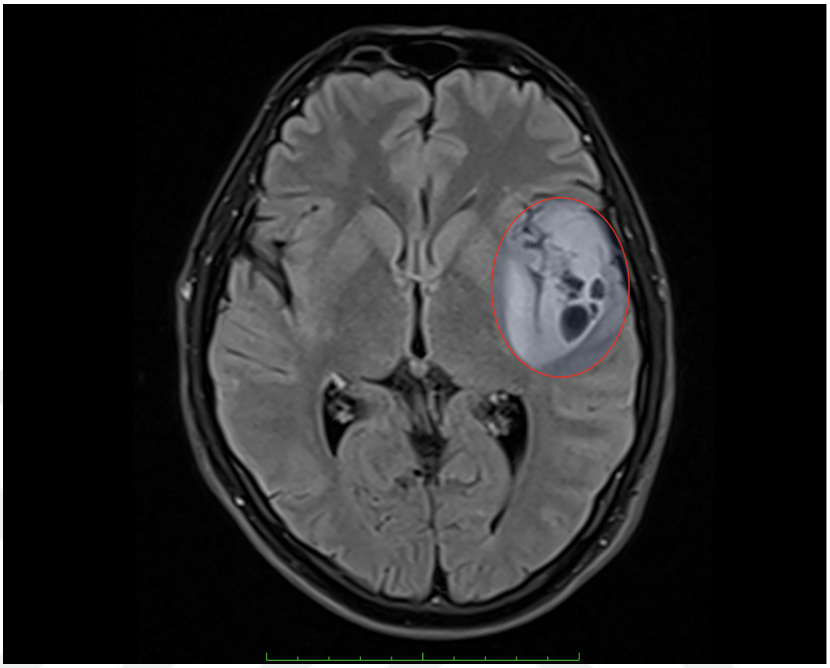

Figure 1.1: A real LGG instance obtained using MRI data located in white matter

[6]. Chemotherapy can be used with or after radiation therapy [7], and its addition to radiation therapy increases both overall survival and progression-free survival [6]. Turning to surgical resection, the standard practice aims to remove the maximum tumor volume possible [6], as greater resection correlates with lower recurrence and higher overall survival rates [3]. Since LGGs are diffusely infiltrative tumors where tumor cell density decreases as a function of distance from the tumor core, it is recommended to adopt maximal safe resection, preserving functioning brain areas [4].

While effective for eliminating tumor tissue, maximum removal approach often fails to account for the brain's complex network structure, where certain regions are critical for overall function. In practice, surgeons lack clear guidelines for balancing tumor removal against functional preservation. This frequently leads to situations where essential brain regions are removed without full understanding of their network importance [8]. Despite the brain's ability to adapt through neuroplasticity, excessive resections can still cause permanent neurological deficits when key connectivity hubs are compromised.

Therefore, understanding the functionality and connectivity of the brain regions is crucial for effective surgical treatment planning. This highlights the need to approach brain tumor resection from an analytical perspective. To this end, several metrics have been proposed in the literature to quantify brain functionality. Leveraging these metrics through analytical methods can help develop more quantitatively informed surgical guidelines, ultimately aiming to preserve healthy brain tissue as much as possible. Accordingly, the motivation of this research is to provide surgeons with a structured and "optimized" resection strategy by modeling the brain as a network and employing mathematical optimization techniques tailored to its unique structure.

1.1 Problem Definition and Solution Approach

This research focuses on LGGs localized in white matter, where tumor occurrence is more prevalent [9]. The slow progression of these tumors suggests that complete resection of all tumorous tissue may not necessarily optimal, as it can cause excessive harm to brain functionality. To address this, we formulate the tumor resection problem as a mathematical optimization model. The model's objective is to maximize post-operative brain functionality while ensuring the total resected tumorous volume exceeds a predefined threshold. To ensure that the resected tumorous region is clinically realistic and spatially connected, the model imposes contiguity constraints.

The human brain is one of the most complex systems known to science, responsible for enabling speech, processing information, memory, and emotional experience. It contains approximately 86 billion neurons, which are specialized cells that transmit information throughout the brain and body [10]. Each neuron consists of a cell body and synapses—the connections through which neurons communicate with one another via electrical and chemical signals. The cell bodies of neurons are located in the gray matter, which forms the brain's outer layer, while the synaptic connections form the white matter, located beneath the gray matter [11]. The Figure 1.2 shows the distinction between the white matter and

the gray matter.

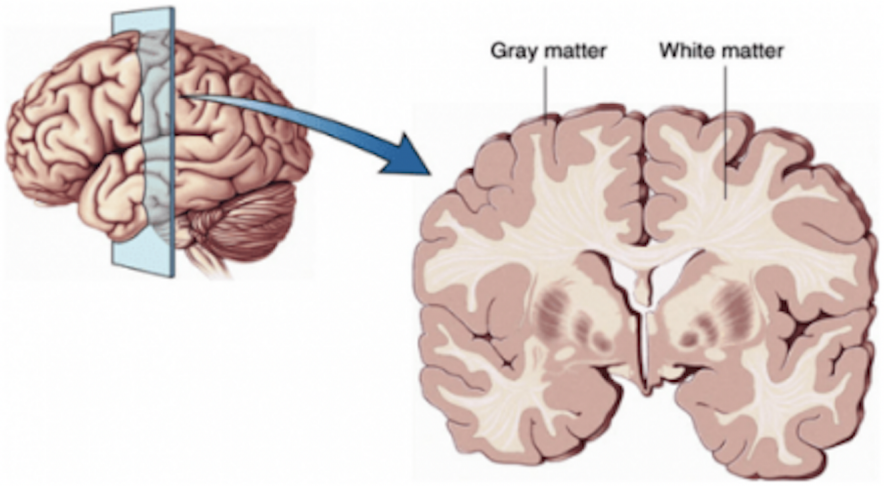

Figure 1.2: A brain white matter and gray matter illustration from a cross section [1]

Different regions of our brain communicate via electrical impulses to enable functional tasks such as visual recognition, language and emotion. Understanding how these regions interact is crucial to have a more thorough knowledge of how our brains work. An important project initiated towards this goal is the Human Connectome Project (HCP), which aims to create a complete mapping of the structural and functional connectivity of an organism's nervous system [12]. To this end, recent advances in medical imaging technologies such as diffusion weighted MRI (dMRI) and functional MRI (fMRI) allowed researchers to probe the neural circuitry of human brains with high spatio-temporal resolution and analyze the structural connectivity and functional correlations between different regions of interest (ROIs) in the human brain [13, 14].

1.1.1 Brain as a Network

To study and analyze the brain in a computational setting, it is essential to first model it as a network. Neuroimaging techniques such as diffusion MRI (dMRI)

and functional MRI (fMRI) not only provide insights into the brain's structure and function, but also enable the representation of the brain as a complex network. Structural connectivity is typically inferred from dMRI using tractography algorithms, which trace white matter pathways between regions of interest (ROIs) [15]. Functional connectivity, on the other hand, is derived from fMRI by measuring correlations in neural activity across different brain regions. Together, these modalities allow researchers to build computational models that capture both anatomical and functional interactions in the brain.

The brain's biological structure—composed of neuron cell bodies and the axonal fibers that link them—naturally lends itself to a network-based representation. The cell bodies are represented as nodes, and the axonal fibers between them serve as the edges of the network [16].

Within this framework, nodes are typically localized in the gray matter, which contains the neuron cell bodies, while edges correspond to connections located in the white matter. The brain network is constructed using voxel-level data, where both edges and nodes are mapped to specific spatial units. However, since voxels represent the smallest structural elements in neuroimaging and their number is extremely high, directly working at the voxel level is computationally infeasible for large-scale modeling. To address this, parcellation techniques [17, 18, 19] to group voxels into larger, functionally or anatomically meaningful units are applied. After parcellation, each of these units is referred to as a region of interest (ROI).

To better reflect the spatial organization and underlying biological roles of brain regions, we categorize the ROIs into two types: GrayROIs (GROIs), which are associated with gray matter and typically serve as the nodes in our network, and WhiteROIs (WROIs), which correspond to white matter regions and are used for modeling the paths traversed by edges. Although edges themselves are not physical regions, they propagate through specific zones of the white matter. For analytical purposes, we divide the white matter into spatial subregions and record which subregions each edge pass through. This spatial decomposition enables us to link edge-level connectivity information to the physical organization of

white matter, which is particularly important in applications like tumor resection planning.

To quantify brain functionality, we use a metric called Global Efficiency (GE). This measure captures how efficiently information can travel across the entire brain network. In simpler terms, it reflects how quickly and effectively different brain regions can communicate with each other. If information can flow along short and direct paths between regions, the brain is considered to be more functionally efficient. If the paths are long or indirect, that might indicate slower communication and reduced coordination. In the context of brain networks, it is commonly used to quantify the brain's overall ability to support parallel information flow and coordinated processing between different regions [20]. Reduced global efficiency has been linked to impairments in brain function. For example, Alzheimer's disease is a well-documented case demonstrating decreased global efficiency in brain networks [21]. Therefore, higher GE values indicate better functional integration of the brain network. It is inversely related to the shortest path distances between nodes, meaning that shorter paths contribute to higher GE values and thus more efficient information transfer. Formally, GE is defined as follows:

$$GE = \frac{1}{|N| \times (|N| - 1)} \sum_{i \in N} \sum_{j \in N, i \neq j} \frac{1}{d_{ij}} \quad [22] \tag{1.1}$$

where d_{ij} is defined as the shortest path between the nodes i and j and N is the set of nodes. As the formulation indicates, GE is inversely proportional to the shortest paths between the nodes in the brain. In the context of brain tumor resection problem, this formula helps us evaluate how well the network supports communication after certain regions (i.e., tumorous areas) are removed.

To quantify tumor impact, we introduce a density metric that measures the extent of damage in affected regions (detailed in subsequent sections). The model incorporates critical surgical constraints, including contiguity requirements for resected regions, reflecting real-world surgical feasibility where scattered removals

are impractical. By integrating these clinical and topological considerations, the model provides a systematic framework for optimizing the balance between tumor removal and functional preservation, offering a systematic approach to complement current resection practices.

Formally, we introduce the following mathematical model for the brain tumor resection problem.

$$\max \quad \mathcal{E}(G \setminus \mathcal{R}) \tag{1.2a}$$

subject to

$$|\mathcal{R}| \geq \Delta, \tag{1.2b}$$

$$\mathcal{R} : \text{contigious} \tag{1.2c}$$

where G is the graph representation of the brain, and $\mathcal{R}$ is the set of WROIs selected for removal during tumor resection. In the objective function 1.2a, we maximize a chosen network connectivity metric, denoted by $\mathcal{E}(\cdot)$, computed on the remaining graph $G \setminus \mathcal{R}$. In this study, we focus on distance-based connectivity measures such as Global Efficiency. Constraint 1.2b ensures that the resected region meets a predefined minimum volume threshold Δ. Constraint 1.2c enforces contiguity of the selected WROIs, reflecting surgical feasibility, as real-world tumor resections cannot involve disconnected regions.

1.2 Literature Review

Understanding the brain requires interdisciplinary efforts that span neuroscience, medical imaging, and computational modeling. This section reviews the essential neuroscience background that introduces the problem and the operations research tools that support its solution.

Neuroscience Literature

To understand the structure and functioning of the brain, it is essential to accurately scan and image it. While Magnetic Resonance Imaging (MRI) provides detailed anatomical information, advancements in imaging technologies—such as

diffusion-weighted MRI (dMRI) and functional MRI (fMRI)—have significantly enhanced our ability to analyze both structural and functional aspects of the brain. One of the foundational studies in Diffusion Tensor Imaging (DTI), a specific application of dMRI, was conducted by Basser et al. [13] . In their work, they introduce a framework for estimating the diffusion of water molecules within a voxel, allowing for the reconstruction and visualization of white matter tracts. This technique is crucial for understanding the connectivity patterns in the brain, especially within white matter.

fMRI, on the other hand, is a non-invasive, high-resolution imaging tool that measures brain activity by detecting changes associated with blood oxygenation levels. It enables researchers to explore brain connectivity by capturing functional correlations between different regions [23, 24]. One notable large-scale initiative that utilizes fMRI for mapping brain connectivity is the Human Connectome Project (HCP). This project aims to improve human neuroimaging techniques and provide a comprehensive understanding of the structural and functional connections in the brain [24, 25].

Apart from imaging techniques to understand brain connectivity, it is also essential to examine the brain's network structure. Bullmore and Sporns [16] argue that the brain exhibits key characteristics of complex networks, both in its functional and structural organization. They emphasize important network properties such as modularity, clustering, and characteristic path length, and explain their functional significance in supporting efficient communication and information processing within the brain. Rubinov and Sporns [26] discuss how brain networks can be constructed from imaging-based connectivity data, and provide a comprehensive overview of commonly used network measures—such as degree, betweenness, and Global Efficiency—which are widely adopted in neuroscience to assess brain function.

Beyond the study of brain connectivity and network organization, it is also crucial to review the clinical literature on brain tumor treatment, particularly the current strategies and technologies used in surgical resection. In current clinical practice, the primary treatment strategy for brain tumors—particularly LGGs

centers around surgical resection. To enhance tumor detection and improve the precision of resection, various techniques have been introduced. Picart et al. [27] examine the use of macroscopic fluorescence techniques to improve intraoperative identification of tumorous tissue, highlighting their advantages in LGG surgeries. However, recognizing that fluorescence-guided methods may fall short in certain cases, Chen et al. [28] propose a PET/NIR dual-modality imaging technique to increase tumor detection accuracy where standard fluorescence fails. Despite the progress in imaging technologies such as diffusion MRI (dMRI), PET, and fluorescence-based approaches, Belsuzarri et al. [29] emphasize that these tools alone are not sufficient and argue for more structured, guided strategies to improve resection outcomes.

In parallel with advancements in tumor detection and resection techniques, functional preservation remains a critical priority, especially because LGGs tend to develop in or near eloquent regions of the brain responsible for speech, motor control, and cognition. To protect these areas, clinicians often rely on intraoperative cortical stimulation and longitudinal neurocognitive testing to map and monitor function during surgery [30, 31]. In addition to these well-established techniques, Henderson et al. [32] highlight how structural connectomes can further support safer and more effective surgical planning. By reviewing the use of diffusion tractography to visualize white matter tracts, they introduce the concept of connectomic imaging as a promising direction for glioma surgery.

Given the limitations of conventional imaging and the need for functionally informed resection strategies, recent efforts have increasingly focused on incorporating functional connectome data into surgical planning workflows. Sparacia et al. [33] demonstrate the importance of evaluating the functional connectome, showing that resting-state fMRI can map brain functionality both before and after surgery. Chen et al. [34] review how gliomas affect both structural and functional connectomes, and they highlight the potential of integrating connectome data with AI to support surgical decision-making. Wei et al. [35] focus on quantifying tumor disruption using structural connectomes and show how connectome-based features can be used to predict overall survival. While their study focuses on glioblastoma, the methodology can be adapted to LGGs to better

assess tumor spread and functional impact. Shah et al. [36] explore how structural and functional connectome imaging can be used to identify critical networks at risk during frontal lobe tumor resections. Their findings emphasize the value of connectome data for preserving functional areas and enabling more precise surgical strategies. Herbet et al. [37] use preoperative connectome features and machine learning techniques to predict cognitive outcomes after glioma surgery. Their work highlights the inherent challenge of balancing tumor resection with functional preservation.

These approaches help define the surgical boundaries more precisely, highlighting the need for data-driven strategies that do not merely focus on anatomical tumor margins but also account for functional connectivity. This motivates the use of brain network models that can support resection planning from both structural and functional perspectives. Modeling the brain as a network and leveraging this model in the surgical decision-making process is an emerging and complementary strategy. Samuel et al. [38] review how functional brain network modeling can inform surgical planning by highlighting critical regions for cognitive function, thus helping to preserve functionality post-operation. Their work emphasizes that integrating network-based insights into preoperative planning can significantly enhance both tumor detection and preservation of neurological outcomes.

Operations Research Literature

While the neuroscience literature provides robust tools for imaging and analyzing the brain's structural and functional characteristics, it often lacks formal methodologies for translating these insights into actionable surgical strategies. Conversely, the operations research community has developed sophisticated optimization frameworks capable of identifying critical elements in network-based systems under a variety of constraints. In this section, we review those methodologies and how they relate to our problem.

In our research, we aim to identify tumorous WROIs whose removal enables resecting a specified volume of tumor tissue while minimizing the resulting decrease in the brain's Global Efficiency, thereby preserving post-operative functionality. While this problem is naturally aligned with the Critical Node Detection Problem

(CNDP)—which focuses on identifying nodes whose removal causes the greatest disruption to network connectivity [39, 40]—it is also closely related to the Critical Edge Detection Problem (CEDP), which seeks to identify the most impactful edges. Our decision variables are defined over WROIs—spatially localized regions derived from white matter structure—they influence the network through the removal of associated edges, making edge-level disruptions highly relevant for assessing functional impact. Veremyev et al. [41] propose an edge-based model that identifies critical connections based on their effect on closeness centrality, a metric closely tied to the global efficiency metric we use. In their model, they minimize the closeness centrality while limiting the number of edges removed. Lalou et al. [40] provide a comprehensive review of CNDP methods, including exact and heuristic approaches. Additionally, Veremyev et al. [42, 41] present a distance-based CNDP/CEDP formulations that serves as the foundation for the models we propose in this thesis. While their work adopts an adversarial perspective aimed at damaging the network, we adapt the same principles constructively, seeking to retain functionality under surgical constraints.

The majority of CNDP/CEDP research—including the works of Veremyev et al. [42] and Arulselvan et al. [39]—employ Mixed Integer Programming (MIP) to model the combinatorial nature of the problem. In these formulations, binary decision variables represent node removal, while constraints capture network structure and connectivity metrics. The MIP approach enables precise modeling of complex objectives such as minimizing pairwise connectivity or distance-based measures, although it often suffers from computational intractability for large-scale instances. Our work builds upon these principles by adapting MIP-based formulations. Moreover, Boginski et al. [43] demonstrate a real-world application of CNDP in the context of protein–protein interaction networks, where the objective is to identify nodes whose removal maximally impairs biological connectivity. This study highlights the practical utility of CNDP in biological settings, making it a particularly relevant example for our work on modeling the brain's structural network under tumor resection.

While our objective is to identify the set of tumorous WROIs whose removal would least impact the overall brain functionality, we also incorporate additional

constraints to ensure surgical feasibility. One of the key constraints is spatial contiguity. In the context of brain tumor surgery, it is clinically necessary for the resected regions to be spatially contiguous, as scattered removal of disconnected tissue does not align with standard surgical practice and safety considerations. To address this, we draw on relevant work in the literature. Wang et al. [44] study the connected subgraph polytope of a graph, providing a general framework for modeling connectivity that can be extended to more constrained problems like ours. Similarly, Carvajal et al. [45] introduce a linear programming-based approach to impose connectivity constraints through the use of minimum cut formulations. Although their work is applied in forest planning, the methodology they propose is well-suited to our setting, where ensuring the physical connectivity of resected white matter regions is critical.

Despite significant advancements in both brain imaging technologies and network-based modeling approaches, there is an obvious lack of interdisciplinary methodologies that combine these tools for real-world neurosurgical decision-making. Existing neuroscience studies focus primarily on structural or functional characterization, while operations research models often overlook the anatomical and surgical constraints specific to the human brain. In particular, LGG resection lacks optimization models that jointly consider (i) functional network preservation, (ii) spatial contiguity of resected regions, and (iii) resected tumorous volume. Our research addresses this lack of systematic approach by developing an optimization framework that integrates surgical expectations with mathematical optimization techniques.

1.3 Contributions

- ***Mathematical Optimization Formulation for Brain Tumor Resection Problem***

  In the context of white matter tumors, the maximal resection approach often lacks systematic guidance. Surgical decisions are typically made without considering the brain's network structure. Our research addresses this

gap by proposing the first mathematical optimization model specifically designed for white matter tumor resection, incorporating the brain's connectivity into the decision-making process.

- ***Imposing Contiguity Constraints***
  From a surgical standpoint, it is important that the regions to be removed are spatially contiguous. To the best of our knowledge, this consideration has not been formally addressed in previous literature. In our study, we explicitly impose physical contiguity constraints, aligning the model's output with what is expected and feasible in surgical practice.

- ***Fast and Scalable Aggregation Heuristic***
  A higher-resolution brain network offers more precise and realistic decisions. However, as the number of ROIs increases, traditional optimization approaches—especially those based on critical node/edge removal—can become computationally expensive. To overcome this, we developed an aggregation heuristic that allows for an increase in both the number of nodes and edges while preserving essential structural information. Our analysis shows that this method is both scalable and efficient, enabling larger problem instances to be solved effectively without compromising decision quality.

- ***Results with Comprehensive Analyses***
  We provide extensive results on both real and synthetic brain instances, offering a thorough analysis that supports the effectiveness of our approach. The diversity of test cases ensures that our methods are robust and adaptable to various conditions. Additionally, by evaluating a wide range of scenarios, we assess whether our model produces outcomes that align with clinical expectations—an important step toward validating its practical relevance.

- ***Bridging Theoretical Modeling with Clinical Insights***
  Our approach was developed in close consultation with domain experts, ensuring that the optimization model reflects realistic surgical priorities and anatomical constraints. By aligning theoretical modeling with practical concerns, the study enhances its relevance and applicability in real-world

clinical settings.

The rest of the paper is organized as follows. In Section 2, we present our modeling approach and introduce the formal mathematical optimization models, along with the additional constraints and methodologies used. Section 3 describes our solution strategy, with a focus on the aggregation heuristic. In Section 4, we detail the experimental setup and report the results of our experiments, including their analysis. Finally, Section 5 concludes the paper and discusses potential directions for future works.

Chapter 2

Modeling Choices

Our modeling process begins by parcellating the brain into WROIs and GROIs. We then map the edges to record which edges pass through which WROIs and which pairs of GROIs they connect. This allows us to systematically determine which connections (streams) would be lost following the resection of a given WROI, and which GROIs would consequently become disconnected.

Figure 2.1 provides a simplified example using a real tumor image. In this figure, nodes 1, 2, and 3 represent GROIs, green lines represent the streams and the overlaid red squares represent the WROIs intersecting the tumorous area. If WROI 1 is removed, no connections are disrupted because no stream passes through it. If WROI 2 is removed, the stream passing through it between GROIs 1 and 3 is cut. Since this was the only stream connecting them, the edge between GROIs 1 and 3 is removed. However, removing WROI 3 cuts one of the streams between GROIs 1 and 2, but another stream connecting them remains intact. Thus, the edge between GROIs 1 and 2 persists.

As it is also introduced in Section 1.2, one influential approach to identifying critical structures in a network is the critical edge detection model introduced by Veremyev et al. [41]. Their model aims to identify a subset of edges whose removal causes the maximum disruption to the network's closeness centrality. By

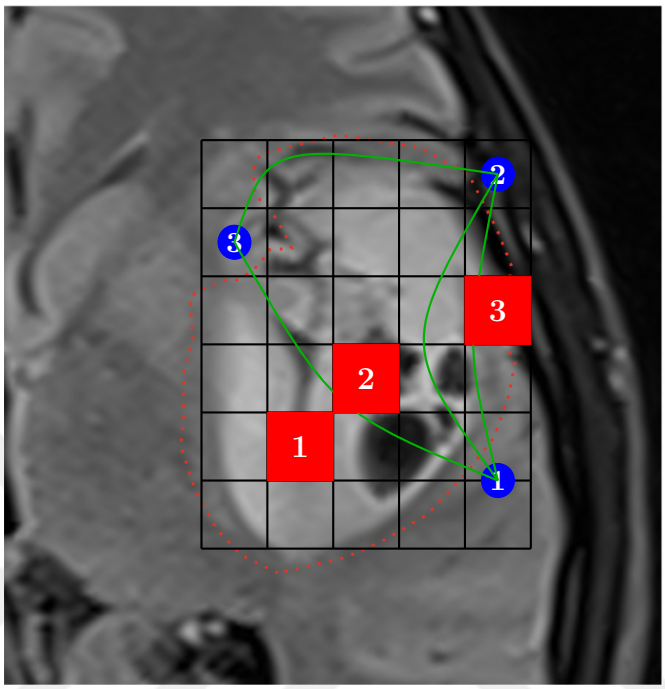

Figure 2.1: Illustrative example over a real tumor image

minimizing the average inverse shortest-path distances among nodes, the model targets connectivity degradation from an adversarial standpoint. The model they introduce is as follows:

Sets

- V: Set of nodes in the network.
- $E \subseteq V \times V$: Set of undirected edges between nodes.
- $S \subseteq V$: Subset of nodes that is of interest to the decision maker.
- L: Maximum number of hops considered for approximating reachability.

Decision Variables

- $y_{ij} \in \{0, 1\}$: Equals 1 if edge $(i, j) \in E$ is removed, 0 otherwise.
- $u_{is}^{(\ell)} \in \{0, 1\}$: Equals 1 if node i is reachable from source s within ℓ hops or fewer, 0 otherwise.

Parameters and Functions

- $f(\ell)$: A nonincreasing function assigning weights to reachability at hop ℓ, used to approximate closeness centrality.
- b: Edge removal budget, i.e., the maximum number of edges that can be deleted.

Model [41]

$$\min_{u,y} \quad \frac{1}{|S|} \sum_{s \in S} \sum_{i \in V} \sum_{\ell=1}^{L} f^{(\ell)} \left(u_{is}^{(\ell)} - u_{is}^{(\ell-1)} \right) \tag{2.1}$$

$$\text{s.t.} \quad u_{is}^{(\ell)} \geq u_{ts}^{(\ell-1)} - y_{it} \qquad \forall s \in S,\ (i,t) \in E,\ \ell \in \{1, \ldots, L\} \tag{2.2}$$

$$u_{is}^{(\ell)} \geq u_{is}^{(\ell-1)} \qquad \forall i \in V,\ s \in S,\ \ell \in \{1, \ldots, L\} \tag{2.3}$$

$$u_{ss}^{(0)} = 1 \qquad \forall s \in S \tag{2.4}$$

$$u_{is}^{(0)} = 0 \qquad \forall i \in V \setminus \{s\},\ s \in S \tag{2.5}$$

$$\sum_{(i,j) \in E} y_{ij} \leq b \tag{2.6}$$

$$u_{is}^{(\ell)},\ y_{ij} \in \{0, 1\} \qquad \forall i \in V,\ s \in S,\ (i,j) \in E,\ \ell \in \{0, \ldots, L\} \tag{2.7}$$

The objective function (2.1) minimizes the weighted sum of reachability across all node pairs (i, s) and path lengths ℓ. The weight function $f(\ell)$ assigns importance to paths based on their length, typically giving higher weight to shorter paths to reflect closeness centrality. By minimizing this sum, the model seeks to damage as much of the network's closeness centrality as possible after edge removals [41].

Constraints (2.2) ensure that node i is reachable from source node s within ℓ hops if there exists a neighboring node t such that t is reachable from s within

$\ell - 1$ hops, and the edge (i, t) is not removed (i.e., $y_{it} = 0$). Constraints (2.3) enforce that if node i is reachable from source s within $l - 1$ hops or fewer, it is also possible to reach node i from source s within l hops or fewer as well. So this constraint ensures that reachability is nondecreasing with respect to the number of hops. If node i is reachable from s within $\ell - 1$ hops, it must also be reachable within ℓ hops. Constraint sets (2.4) ensure that each source node s is trivially reachable from itself with zero hops. Constraint sets (2.5) ensures that all nodes other than the source node s are not reachable from s within zero hops. Constraints (2.6) limits the total number of edges removed to the given budget b. Constraints (2.7) ensure the decision variables $u_{is}^{(\ell)}$ and y_{ij} are binary [41].

This model, finds the edges whose removal would decrease the central closeness at most. While this framework proposed by Veremyev et al. [41] serves as the foundational basis for our formulation, our model differs in several crucial ways due to the specific characteristics of brain networks and surgical constraints.

In the context of brain surgery, especially within white matter, the anatomical reality is that streams—representing neural connections or fiber tracts—are not isolated structures that can be selectively removed. These streams are embedded within physical brain tissue, and disrupting them requires resecting a region through which the fibers pass. Thus, instead of targeting streams directly, our model focuses on the resection of WROIs.

To account for this difference, we introduce several additional parameters and modeling steps. Specifically, as it was shown in the example above when a WROI is resected, all streams passing through it are cut. Consequently, for any pair of GROIs connected by these streams, their connectivity is reduced by the number of streams cut. If all streams between a pair of GROIs are cut (i.e., no streams remain), the edge between them is removed from the brain network. Otherwise, the edge persists as long as at least one stream survives.

To mathematically capture these dynamics, we define a_{sk} to indicate whether edge s passes through WROI k, e_{ij}^{s} to represent whether stream s connects GROIs i and j, and w_{ij} as the total number of streams connecting GROIs i and j. These

parameters allow us to encode how the removal of certain regions impacts the structure and function of the brain network, differentiating our model fundamentally from prior work.

In addition to this structural shift from edge removal to region removal, another key departure lies in our objective: whereas Veremyev et al. [41] aim to minimize network efficiency by targeting critical edges, our goal is to maximize efficiency under minimum resection constraints. This reflects the clinical context of our application—where the aim is not to damage the network but to preserve its function as much as possible despite necessary tumor-related resections. By modeling the optimization in this way, we prioritize the maintenance of communication between brain regions, aligning the mathematical objective with the neurological goal of preserving cognitive and motor function post-surgery.

2.1 Mathematical Model

Using the conceptual model described above, we construct the following mathematical model to formalize our approach. Unlike traditional edge-centric formulations, our model explicitly incorporates removal of WROIs as decision variables, reflecting a more anatomically and surgically realistic representation of tumor resection. By modeling how the removal of specific regions impacts connectivity—rather than removing abstract edges—we align our optimization structure with clinical constraints and capabilities. We begin with introducing Sets, Parameters, Decision Variables used throughout different formulations proposed.

Sets and Indices

$\mathcal{N} = \{1, \ldots, \text{nb\_grois}\}$ Set of GROIs

$\mathcal{S} = \{1, \ldots, \text{nb\_streams}\}$ Set of streams

$\mathcal{K} = \{1, \ldots, \text{nb\_wrois}\}$ Set of WROIs

$\mathcal{L} = \{1, \ldots, L\}$ Set of layers

$\Gamma(u, v) = \{S \subseteq \mathcal{K} \setminus \{u, v\} : S \text{ is a minimal } uv\text{-node cut}\}$

$\mathcal{T} =$ Set of Tumorous ROI's

Parameters

$$a_{sk} = \begin{cases} 1, & \text{if stream } s \text{ passes through WROI } k \quad s \in \mathcal{S}, k \in \mathcal{K} \\ 0, & \text{otherwise} \end{cases}$$

$$b_{kl} = \begin{cases} 1, & \text{if GROIs } k \text{ and } l \text{ are spatially neighbors} \quad k, l \in \mathcal{N} \\ 0, & \text{otherwise} \end{cases}$$

$$e_{ij}^{(s)} = \begin{cases} 1, & \text{if the endpoints of the stream } s \text{ are in GROIs } i \text{ and } j \quad i, j \in \mathcal{N}, s \in \mathcal{S} \\ 0, & \text{otherwise} \end{cases}$$

$w_{ij} = \sum_{s \in S} e_{ij}^{(s)}$: Number of streams connecting GROIs i and j.

$$g_{ij} = \begin{cases} 1 & \text{if there is a direct edge from i to j, } i, j \in \mathcal{N} \\ 0, & \text{otherwise} \end{cases}$$

$v_0 =$ Minimum volume threshold that must be removed

$N = |\mathcal{N}|$

Decision Variables

$$x_k = \begin{cases} 1, & \text{if the wROI } k \text{ is resected} \quad k \in \mathcal{K} \\ 0, & \text{otherwise} \end{cases}$$

$$z_s = \begin{cases} 1, & \text{if the stream } s \text{ is cut} \quad s \in \mathcal{S} \\ 0, & \text{otherwise} \end{cases}$$

$$y_{ij} = \begin{cases} 1, & \text{if the gROIs } i \text{ and } j \text{ are not connected after resection} \quad i, j \in \mathcal{N} \\ 0, & \text{otherwise} \end{cases}$$

$$u_{ij}^{(l)} = \begin{cases} 1, & \text{if there exists a path of length at most } l \text{ between } i \text{ and } j \text{ after resection} \quad i, j \in \mathcal{N} \\ 0, & \text{otherwise} \end{cases}$$

2.1.1 Base Non-Linear Model

Before presenting our mathematical model, we define the *Global Efficiency (GE)* metric, which serves as our primary optimization objective. Instead of computing shortest path distances directly, we adopt a layered reachability formulation aligned with the framework proposed by Veremyev et al. [42]. For each node pair $(i, j) \in \mathcal{N} \times \mathcal{N}$, we define a binary variable $u_{ij}^{(l)}$, which equals 1 if there exists a path of length at most l between nodes i and j, and 0 otherwise.

Using a non-increasing weighting function $f(l)$, such as $f(l) = 1/l$, we define the global efficiency of the network as:

$$GE(G) = \frac{1}{N \times (N-1)} \sum_{i \in \mathcal{N}} \sum_{j \in \mathcal{N}} \sum_{l=1}^{L} f(l) \left(u_{ij}^{l} - u_{ij}^{l-1} \right) \tag{2.8}$$

This formulation captures the overall efficiency of communication in the network by summing the marginal contributions of all node pairs' shortest distances in the modified (i.e. resected) network. Our optimization model seeks to maximize this GE value after removing a subset of tumorous regions, while ensuring

that the total resected tumor volume exceeds a predefined threshold. The resulting mathematical optimization formulation is as follows.

Objective Function

$$\text{Maximize} \quad \frac{1}{N \times (N-1)} \sum_{i \in \mathcal{N}} \sum_{j \in \mathcal{N}} \sum_{l=1}^{L} f(l) \left(u_{ij}^{l} - u_{ij}^{l-1} \right) \tag{2.9}$$

Constraints

$$\sum_{i \in \mathcal{T}} v_i x_i \geq v_0 \tag{2.10}$$

$$u_{ij}^{l} \leq \sum_{k=1}^{l-1} u_{ij}^{k} + \sum_{t \in \mathcal{N}, t \neq i, t \neq j} (1 - y_{it}) g_{it} u_{tj}^{l-1}, \qquad \forall i, j \in \mathcal{N}, i \neq j, \forall l \in \{2, \ldots, L\} \tag{2.11}$$

$$u_{ij}^{1} \leq (1 - y_{ij}) g_{ij}, \qquad \forall i, j \in \mathcal{N}, i \neq j \tag{2.12}$$

$$z_s \geq \frac{1}{|\mathcal{K}|} \sum_{k \in \mathcal{K}} a_{sk} x_k, \qquad \forall s \in \mathcal{S} \tag{2.13}$$

$$y_{ij} \leq \frac{1}{\mathrm{w}_{ij}} \sum_{s \in \mathcal{S}} e_{ij}^{s} z_s, \qquad \forall i, j \in \mathcal{N}, (\mathrm{i,j}) \in E \tag{2.14}$$

$$\sum_{s \in \mathcal{S}} e_{ij}^{s} z_s - M y_{ij} \leq \mathrm{w}_{ij} - 1, \qquad \forall i, j \in \mathcal{N}, (\mathrm{i,j}) \in E \tag{2.15}$$

$$y_{ij} = 0 \qquad \forall i, j \in \mathcal{N}, (\mathrm{i,j}) \in E, b_{ij} = 1 \tag{2.16}$$

$$u_{ij}^{l} = u_{ji}^{l}, \qquad \forall i, j \in \mathcal{N}, \forall l \in \mathcal{L} \tag{2.17}$$

$$y_{ij} = y_{ji}, \qquad \forall i, j \in \mathcal{N} \tag{2.18}$$

$$u_{ii}^{0} = 1 \qquad \forall i \in \mathcal{N} \tag{2.19}$$

$$u_{ij}^{0} = 0 \qquad \forall i, j \in \mathcal{N}, i \neq j \tag{2.20}$$

$$\sum_{w \in S} x_w \geq x_u + x_v - 1, \qquad \forall S \in \Gamma(u, v), \quad \forall u, v \in \mathcal{K} \tag{2.21}$$

$$x_k \in \{0, 1\} \qquad \forall k \in \mathcal{K} \tag{2.22}$$

$$z_s \in \{0, 1\} \qquad \forall s \in \mathcal{S} \tag{2.23}$$

$$u_{ij}^{l} \in \{0, 1\} \qquad \forall i, j \in \mathcal{N}, l \in \mathcal{L} \tag{2.24}$$

$$y_{ij} \in \{0, 1\} \qquad \forall i, j \in \mathcal{N} \tag{2.25}$$

The objective function (2.9) maximizes global efficiency where u_{ij}^{l} indicates connectivity via paths of length $\leq l$, and $1/N(N-1)$ is the normalization term for all possible pairs.

Constraint (2.10) ensures the removed tumor volume exceeds a specified threshold. The constraints (2.11) recursively define whether a path of length at most l exists between nodes i and j. Specifically, the variable u_{ij}^{l} is set to 1 if either (i) a path of shorter length (i.e., less than l) already exists between i and j, or (ii) there exists an intermediate node t such that i is directly connected to t (i.e., edge (i,t) is active), and t can reach j within $l-1$ steps. The edge (i,t) is considered functional if $y_{it}=0$, meaning it has not been removed. The binary parameter g_{it} indicates the existence of the edge in the original graph. Constraints (2.12) ensure that if the edge between nodes i and j is removed (i.e., $y_{ij}=1$), then the path length between them cannot be 1. Constraints (2.13) enforce stream removal. Specifically, for each stream s, if any of the WROIs it passes through (identified by a_{sk}) is removed ($x_k=1$) then the stream s must also be considered cut ($z_s=1$). Constraints (2.14) and (2.15) collectively ensure that an edge is considered functional ($y_{ij}=1$) only if at least one of the streams connecting i and j remains uncut. Otherwise, when all connecting streams are removed, the edge must be cut. Constraints (2.16) preserve anatomical (spatial) neighbor connectivity. For node pairs that are spatial neighbors (i.e., $b_{ij}=1$), the model prohibits their disconnection by enforcing $y_{ij}=0$. Constraints (2.17) and (2.18) impose symmetry as the network is undirected. Constraints (2.19) and (2.20) initialize the path length indicators for GE computation. Each node has a zero-length path to itself , while no node has a zero-length path to any other node. Constraints (2.21) ensure spatial contiguity among removed WROIs. If two WROIs u and v are removed, then at least one node from every minimum node cut set separating them must also be removed. This constraint is not embedded directly in the model but added iteratively for each solution, as described in Section 2.1.6. Finally, (2.22), (2.23),(2.24) and (2.25) define the binary nature of variables x_i, z_s, u_{ij}^{l} and y_{ij} respectively.

Notice that the constraint in 2.11, which recursively defines whether a path of length at most l exists between nodes i and j, is nonlinear. This nonlinearity

arises from the multiplication of two decision variables. Specifically, if there is a direct edge between nodes i and t, and node t can reach j within $l-1$ steps, then it would originally imply that node i can reach j within l steps. However, following resection, the edge between i and t may be disrupted. Consequently, node i may no longer reach j within l steps. To capture this possibility, we include a check on whether the edge between nodes i and t still exists, as represented by the decision variable y_{it} and this makes the base model non-linear.

To address the possible computational challenges posed by this nonlinearity, we now introduce an alternative linear formulation.

2.1.2 Base Linearized Model

While the previous non-linear model can be solved by Gurobi (which handles non-linearity to some extent), we investigated whether a linear formulation could improve computational efficiency. This is important as improving the computational efficiency would help us to increase the problem size. Increasing the problem size would also increase the resolution of the brain network and hence yield to more realistic results.

To linearize the non-linear constraint where we multiply decision variables, we use the concept of shortest path trees (SPTs). A shortest path tree rooted at node i is a spanning tree that connects i to all other nodes in the network using the shortest possible paths. In other words, for every node $j \neq i$, the path from i to j in the tree corresponds to a shortest path in the original graph. By modeling these trees, we can represent the distances between nodes in a way that allows us to formulate the problem using only linear constraints. This led to the development of our second model, which required the introduction of new decision variables to maintain functional equivalence while achieving linearity.

Additional Decision Variable

$$v_{jk}^{i} = \begin{cases} 1 & \text{if the shortest path tree rooted at } i \text{ includes arc } (j,k), \\ 0 & \text{otherwise.} \end{cases}$$

Objective Function

$$\text{Maximize} \quad \frac{1}{N \times (N-1)} \sum_{i \in \mathcal{N}} \sum_{j \in \mathcal{N}} \sum_{l=1}^{L-1} f(l) \left(u_{ij}^{l} - u_{ij}^{l-1} \right) \tag{2.26}$$

Constraints

$$\sum_{i \in \mathcal{T}} v_i x_i \geq v_0 \tag{2.27}$$

$$z_s \geq \frac{1}{|\mathcal{K}|} \sum_{k \in \mathcal{K}} a_{sk} x_k, \qquad \forall s \in \mathcal{S} \tag{2.28}$$

$$\sum_{k \neq j} v_{kj}^i = 1, \qquad \forall i, j \in N,\, i \neq j \tag{2.29}$$

$$v_{jk}^i \leq g_{jk}(1 - y_{jk}), \qquad \forall i, j, k \in N,\, j \neq k,\, i \neq k \tag{2.30}$$

$$u_{ik}^l \leq u_{ij}^{l-1} + M(1 - v_{jk}^i), \qquad \forall l \in [2, \ldots, L],\, \forall i, j, k \in N,\, j \neq k,\, i \neq k \tag{2.31}$$

$$u_{ik}^l \geq u_{ij}^{l-1} - M(1 - v_{jk}^i), \qquad \forall l \in [2, \ldots, L],\, \forall i, j, k \in N,\, j \neq k,\, i \neq k \tag{2.32}$$

$$y_{ij} \leq \frac{1}{\mathrm{w}_{ij}} \sum_{s \in \mathcal{S}} e_{ij}^s z_s, \qquad \forall i, j \in \mathcal{N}, (\mathrm{i,j}) \in E \tag{2.33}$$

$$\sum_{s \in \mathcal{S}} e_{ij}^s z_s - M y_{ij} \leq \mathrm{w}_{ij} - 1, \qquad \forall i, j \in \mathcal{N}, (\mathrm{i,j}) \in E \tag{2.34}$$

$$y_{ij} = 0 \qquad \forall i, j \in \mathcal{N}, (\mathrm{i,j}) \in E, b_{ij} = 1 \tag{2.35}$$

$$u_{ij}^l = u_{ji}^l, \qquad \forall i, j \in \mathcal{N}, \forall l \in \mathcal{L} \tag{2.36}$$

$$y_{ij} = y_{ji}, \qquad \forall i, j \in \mathcal{N} \tag{2.37}$$

$$u_{ii}^0 = 1 \qquad \forall i \in \mathcal{N} \tag{2.38}$$

$$u_{ij}^0 = 0 \qquad \forall i, j \in \mathcal{N}, i \neq j \tag{2.39}$$

$$\sum_{w \in S} x_w \geq x_u + x_v - 1, \qquad \forall S \in \Gamma(u, v), \quad \forall u, v \in \mathcal{K}, (u, v) \notin E \tag{2.40}$$

$$x_k \in \{0, 1\} \qquad \forall k \in \mathcal{K} \tag{2.41}$$

$$z_s \in \{0, 1\} \qquad \forall s \in \mathcal{S} \tag{2.42}$$

$$u_{ij}^l \in \{0, 1\} \qquad \forall i, j \in \mathcal{N}, l \in \mathcal{L} \tag{2.43}$$

$$y_{ij} \in \{0, 1\} \qquad \forall i, j \in \mathcal{N} \tag{2.44}$$

$$v_{jk}^i \in \{0, 1\} \qquad \forall i, j, k \in \mathcal{N} \tag{2.45}$$

The objective function in (2.26) maximizes global efficiency, as in the previous non-linear formulation. Several constraints remain unchanged: (2.27) ensures the resected tissue exceeds a minimum volume threshold, and (2.28) models edge disconnection through removed WROIs. The main difference in this model lies in its use of shortest path trees to linearize the path structure. Constraint (2.29) guarantees that for every node i, the corresponding shortest path tree includes

exactly one incoming arc for each other node j, thus enforcing a unique shortest path from i to every j. Constraint (2.30) links tree construction to edge availability: if a stream (edge) between nodes j and k is cut during resection, then that edge cannot be used in any shortest path tree rooted at any node i. Together, constraints (2.31) and (2.32) propagate path length values by ensuring that if node k is reachable from i via j, and the arc (j, k) is part of the shortest path tree rooted at i, then the distance variable u^l_{ik} reflects that connectivity. If the arc (j, k) is not part of the tree, the constraints become inactive due to the large constant M. All remaining constraints mirror those in the previous model and serve the same purposes: defining connectivity loss, preserving variable symmetry, enforcing path initialization, and maintaining spatial contiguity and binary nature of decision variables.

Despite the benefits of linearization, the number of constraints and variables can remain significant. To mitigate this, we turn to the concept of minimal hitting sets, which enables a more compact representation of critical connectivity structures.

2.1.3 Finding Hitting Sets

In the previos formulations, we included binary decision variables to represent whether a stream is cut and whether a GROI pair becomes disconnected following tumor resection. While this formulation is straightforward, the inclusion of these binary variables significantly increases the number of decision variables and constraints in the model, leading to longer computational times and reduced scalability.

To address this, we implement hitting sets as a way to eliminate those auxiliary decision variables while preserving the logical structure of the model. Before introducing our last model, we first need to introduce the hitting set and minimal hitting set concepts. We use minimal hitting sets in order to decrease the number of constraints and decision variables and increase the efficiency in our model.

A hitting set H for a finite family K of finite sets $\{S_1, S_2, \ldots\}$ is a set that intersects every $S_i \in K$. When no proper subset of H satisfies this condition, H becomes a minimal hitting set (MHS) [46].

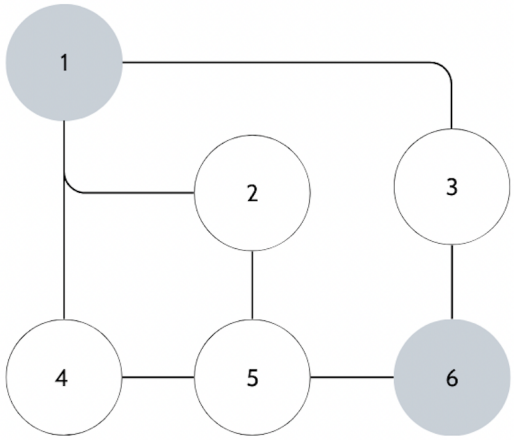

Figure 2.2: An example network used to illustrate the principle of hitting sets

Figure 2.2 illustrates this for node pair (1,6). The path sets $\{\{2,5\},\{3\},\{4,5\}\}$ yield minimal hitting sets $\{\{3,5\},\{2,3,4\}\}$. This means disconnection occurs either when removing both nodes 3 and 5, or when removing nodes 2, 3, and 4.

In our resection framework, hitting sets are used to identify critical WROIs whose removal results in the disconnection of specific GROI pairs.

This implementation involves three key steps. First, for each GROI pair, we map all streams that connect them. Second, we identify and catalog the WROIs through which each of those connecting streams passes. The minimal hitting sets of this collection of WROIs indicate the smallest combinations of WROIs whose removal guarantees the disconnection of the corresponding GROI pair. In this way, we can directly model the disconnection without explicitly introducing binary variables for each stream or pairwise relationship.

To illustrate, consider the example in Figure 2.2, where nodes 1 and 6 are GROIs, and the remaining nodes represent WROIs. For this setup, the minimal hitting sets that sever all paths between GROIs 1 and 6 are $\{\{3,5\},\{2,3,4\}\}$.

This means that if the model chooses to resect either WROIs 3 and 5 together, or WROIs 2, 3, and 4, the connection between GROIs 1 and 6 is successfully disrupted. This approach allows us to encode the same connectivity logic more compactly and efficiently. Using this principle, we derive the mathematical model introduced in Section 2.1.4, where hitting sets serve as the foundation for a more tractable optimization formulation.

For computational implementation, we used PySAT's Hitman module [47, 48] to exhaustively find all minimal hitting sets between GROI pairs, enabling complete network disruption analysis.

2.1.4 Non-Linear Model with Hitting Sets

This model represents our most efficient formulation, where we've eliminated both the z and y variables while preserving the original optimization logic. By removing these binary variables, we significantly reduce computational complexity without altering the model's core functionality. The objective remains maximizing global efficiency through the same path-based metric, but now achieves faster solution times.

To enable this formulation, we define the following set for each pair of nodes:

$\mathcal{H}_{ij} = \{H_{ij}\}$: the set of all minimal hitting sets that disconnect node pair (i, j).

These sets are precomputed for each node pair and integrated into the model as a compact representation of connectivity loss.

Objective Function

$$\text{Maximize} \quad \frac{1}{N \times (N-1)} \sum_{i \in \mathcal{N}} \sum_{j \in \mathcal{N}} \sum_{l=1}^{L} f(l) \left(u_{ij}^{l} - u_{ij}^{l-1} \right) \tag{2.46}$$

Constraints

$$\sum_{i \in \mathcal{T}} v_i x_i \geq v_0 \tag{2.47}$$

$$u_{ij}^k \leq \sum_{l=1}^{k-1} u_{ij}^l + \sum_{t \in \mathcal{N}, t \neq i, t \neq j} u_{it}^1 u_{tj}^{k-1}, \qquad \forall i, j \in \mathcal{N}, i \neq j, \forall k \in \{2, \ldots, L\} \tag{2.48}$$

$$u_{ij}^1 \leq |H_{ij}| - \sum_{s \in \mathcal{H}_{ij}} x_s \qquad \forall i, j \in \mathcal{N}, \forall H_{ij} \in \mathcal{H}_{ij} \tag{2.49}$$

$$u_{ij}^l = u_{ji}^l, \qquad \forall i, j \in \mathcal{N}, \forall l \in \mathcal{L} \tag{2.50}$$

$$\sum_{w \in S} x_w \geq x_u + x_v - 1, \qquad \forall S \in \Gamma(u, v), \quad \forall u, v \in \mathcal{K}, (u, v) \notin E \tag{2.51}$$

$$x_k \in \{0, 1\} \qquad \forall k \in \mathcal{K} \tag{2.52}$$

$$u_{ij}^l \in \{0, 1\} \qquad \forall i, j \in \mathcal{N}, l \in \mathcal{L} \tag{2.53}$$

The objective function (2.46) remains unchanged from previous formulations—it maximizes global efficiency. Constraint (2.47) ensures that the total volume of resected regions remains above a specified threshold v_0. Constraints (2.48) govern the path existence variables. For a node pair (i, j) and a given path length k, if there is no direct path of length k or shorter, and if nodes i and j are not connected through an intermediate node t (where t is directly connected to i and has a path of length $k-1$ to j), then the variable u_{ij}^k is forced to be zero. Conversely, if such paths exist, u_{ij}^k is allowed to take the value 1, and since the model maximizes efficiency, it will do so whenever possible. Constraints (2.49) enforce disconnection via minimal hitting sets: if all nodes in any hitting set for a pair (i, j) are removed, the model sets u_{ij}^1 to 0, effectively cutting the connectivity between i and j. Constraint (2.50) maintains consistency by ensuring that $u_{ij}^k = u_{ji}^k$, reflecting the undirected nature of the network. Constraint (2.51) enforces spatial contiguity among the selected resected nodes, ensuring that the removed regions form a connected subgraph. Finally, constraints (2.52) and (2.53) define the binary nature of the decision variables x_i and u_{ij}^l, respectively.

While the previous models focused on maximizing the GE, we now introduce a Worst Resection Model to identify resections that would cause the greatest possible decline in GE—serving as a benchmark to assess the performance of our

approach.

2.1.5 Worst Resection Model

This model builds upon the Base Nonlinear Model with Hitting Sets introduced in Section 2.1.4. Its goal is to identify the WROIs whose resection would most significantly reduce GE. However, since this model seeks the "worst" resection (in terms of functional damage), it must be constrained to avoid resecting all tumorous regions. Additionally, because the model involves minimization, we made several key modifications to ensure variables behave as intended.

We first introduce the following auxiliary decision variable:

Additional Decision Variable

$$n_{ij}^{g} = \begin{cases} 1 & \text{if not all of the members of a minimal hitting set } H_{ij}[g] \text{ between nodes} \\ & i \text{ and } j \text{ are removed} \\ 0 & \text{otherwise.} \end{cases}$$

where $\mathcal{H}_{ij} = \{\mathcal{H}_{ij}[1], \mathcal{H}_{ij}[2], \ldots \mathcal{H}_{ij}[|\mathcal{H}_{ij}|]\}$

Objective Function

$$\text{Minimize} \quad \frac{1}{N \times (N-1)} \sum_{i \in \mathcal{N}} \sum_{j \in \mathcal{N}} \sum_{l=1}^{L} f(l) \left(u_{ij}^{l} - u_{ij}^{l-1} \right) \tag{2.54}$$

Constraints

$$\sum_{i\in\mathcal{T}} v_i x_i \leq v_0 \tag{2.55}$$

$$u_{ij}^k \leq \sum_{l=1}^{k-1} u_{ij}^l + \sum_{t\in\mathcal{N},t\neq i,t\neq j} u_{it}^1 u_{tj}^{k-1}, \qquad \forall i,j\in\mathcal{N}, i\neq j, \forall k\in\{2,\ldots,L\} \tag{2.56}$$

$$u_{ij}^k \geq \frac{\sum_{l=1}^{k-1} u_{ij}^l + \sum_{t\in\mathcal{N},t\neq i,t\neq j} u_{it}^1 u_{tj}^{k-1}}{M} \qquad \forall i,j\in\mathcal{N}, i\neq j, \forall k\in\{2,\ldots,L\} \tag{2.57}$$

$$n_{ij}^g \leq H_{ij}[g]| - \sum_{s\in\mathcal{H}_{ij}[g]} x_s \qquad \forall i,j\in\mathcal{N}, \forall H_{ij}[g]\in\mathcal{H}_{ij} \tag{2.58}$$

$$n_{ij}^g \geq \frac{|H_{ij}[g]| - \sum_{s\in H_{ij}[g]} x_s}{|H_{ij}[g]|} \qquad \forall i,j\in\mathcal{N}, \forall g\in\{1,\ldots,|\mathcal{H}_{ij}|\} \tag{2.59}$$

$$u_{ij}^1 \geq \sum_{g=1}^{|H_{ij}|} n_{ij}^g - |H_{ij}[g]| + 1 \qquad \forall i,j\in\mathcal{N}, \forall H_{ij}\in\mathcal{H}_{ij} \tag{2.60}$$

$$u_{ij}^l = u_{ji}^l, \qquad \forall i,j\in\mathcal{N}, \forall l\in\mathcal{L} \tag{2.61}$$

$$\sum_{w\in S} x_w \geq x_u + x_v - 1, \qquad \forall S\in\Gamma(u,v), \quad \forall u,v\in\mathcal{K}, (u,v)\notin E \tag{2.62}$$

$$x_k \in \{0,1\} \qquad \forall k\in\mathcal{K} \tag{2.63}$$

$$u_{ij}^l \in \{0,1\} \qquad \forall i,j\in\mathcal{N}, l\in\mathcal{L} \tag{2.64}$$

$$y_{ij} \in \{0,1\} \qquad \forall i,j\in\mathcal{N} \tag{2.65}$$

The objective function (2.54) is formulated to minimize global efficiency, as our aim here is to identify the most functionally damaging resection. Constraint 2.55 ensures that the resected tumor volume does not exceeds a given threshold, thereby preventing the model from trivially removing all tumor regions.

Constraints (2.56) and (2.57) handle path existence in the network. While (2.56) is inherited from the base model, the minimization objective in this case introduces new behavior: unless explicitly enforced, binary path variables (u) will tend toward 0 to improve the objective. To counter this, (2.57) forces u_{ij}^k to be 1 when a valid path of length k exists via either shorter paths or through an

intermediate node t.

Similarly, the logic behind hitting sets must also be reversed. In the maximization model, if all nodes in a minimal hitting set between nodes i and j are removed, the corresponding edge is lost, and u_{ij}^1 naturally drops to 0 without additional constraints. But in this worst-case model, if the connection still exists, we must actively enforce $u_{ij}^1 = 1$ whenever at least one node in the hitting set remains. Constraints (2.58) and (2.59) ensure that the auxiliary variable n_{ij}^g is 1 if at least one node from a given hitting set $\mathcal{H}ij$ remains, and 0 otherwise. Then, constraint (2.60) ensures that uij^1 equals 1 if all hitting sets for the node pair (i, j) are still partially intact.

The rest of the constraints—(2.61),(2.62), (2.63), (2.64), and (2.65)—mirror those in the original best resection model and ensure consistency in symmetry, contiguity, and variable domains.

To explore potential improvements in computational efficiency, we also developed two alternative formulations. The first, presented in Appendix A, eliminates the binary variables z while keeping the variables y, by incorporating hitting set constraints, aiming to simplify the model structure. The second, detailed in Appendix B, removes the binary variables y to reduce the overall problem size. While both formulations offer valuable insights into the design space of the model, they did not perform as well as the Non-Linear Model with Hitting Sets in terms of scalability.

2.1.6 Enforcing Contiguity

Spatially contiguous resection is a clinical requirement in brain tumor surgeries, and therefore it must be properly incorporated into our model. To enforce spatial contiguity, we adopt the connectivity constraints introduced by Carvajal et al. [45]. This corresponds to the constraints (2.21), (2.40) and (2.51) in the models Base Non-Linear Model, Base Linearized Model and Non-Linear Model with Hitting Sets, respectively. However, directly embedding all of these constraints

into the optimization model significantly increases the problem size, which makes solving the model intractable for large-scale networks—such as the brain network—where the number of nodes and edges is substantial.

To address this challenge, we implement a separation-based approach that selectively adds contiguity constraints only when necessary. More specifically, after obtaining an integer solution $\mathcal{R}$ from the optimization model—without initially including the contiguity constraints—we analyze this solution to identify potential violations of spatial connectivity. For each pair of removed nodes i and j in the solution $\mathcal{R}$ (where $i, j \in \mathcal{T}$), we solve a separation problem. To construct the problem between two removed nodes i and $j \in \mathcal{T}$, the methodology described in Carvajal et al. [45] is followed. After we find the minimum cut between nodes i and j, we use that min-cut to integrate the contiguity constraint. We repeat the same process each time a solution $\mathcal{R}$ is found. When a solution $\mathcal{R}$ is found that does not violate the contiguity constraints, the optimal solution is reached.

Chapter 3

Solution Approach

The original model can become computationally intensive to solve, especially when the number of nodes and connections in the network increases. Among all components, the number of GROIs (gray matter regions of interest) presents the greatest scalability challenge. Since each GROI introduces additional decision variables and connectivity considerations, the problem size grows rapidly with their count. To mitigate this issue, we introduce an aggregation heuristic that reduces complexity while maintaining spatial coherence. GROIs are clustered based on their spatial coordinates using the Clauset-Newman-Moore greedy modularity maximization method [49], which allows us to treat each cluster as a single aggregated node in the model. WROIs, on the other hand, are left unaggregated to ensure that tumor regions retain their detailed structure and are modeled with full resolution.

Aggregation Heuristic

The core mechanism of our aggregation heuristic is formalized in Algorithm 1 and illustrated in Figure 3.1.

As detailed in Algorithm 1, the aggregated graph is constructed through four key phases. First, each identified community of GROIs is merged into a single super-node that preserves the spatial and topological properties of the original

Algorithm 1 Aggregation Heuristic

Given streams $\mathcal{S}$ and a spatial connectivity graph $G = (V, E)$ with GROIs V
Use the Clauset-Newman-Moore greedy modularity maximization method to create communities $\mathcal{C}$ over the GROIs
Initialize the spatial connectivity graph $G' = (\mathcal{C}, E')$ over the communities
for each community $v \in \mathcal{C}$ **do**
    Identify the neighboring GROIs of each member of v using the original graph G
    for each community $u \in \mathcal{C}$ **do**
        if $u \neq v$ **and** any member of u is a neighbor of any member of v **then**
            Add an edge between communities u and v in G'
        end if
    end for
end for
Initialize $G'' = (\mathcal{C}, E'')$ as the inter-community connectivity graph and define the connection count matrix $NB' \in \mathbb{N}^{|\mathcal{C}|\times|\mathcal{C}|}$
for each stream $s \in \mathcal{S}$ **do**
    Determine the start and end GROIs of stream s and map them to their respective communities $i, j \in \mathcal{C}$
    if $i \neq j$ **then**
        Add an edge between communities i and j in G''
        Increment NB'_{ij} (number of connections between communities i and j)
    end if
end for
Using G', G'' and NB'_{ij} solve the model introduced in Section 2.1.4
Using the resulting resected WROIs from the aggregation heuristic solution, calculate the GE of the original graph G

community. These super-nodes reflect the collective behavior of their constituent nodes while reducing graph complexity. Second, spatial connectivity is preserved by adding edges between communities that share spatial adjacency in the original graph. Third, inter-community connectivity is preserved by establishing edges between super-nodes according to the original stream-level interactions. Finally, tumor-infiltrated WROIs remain unaggregated to retain their anatomical boundaries and pathological characteristics without modification. This four-stage process yields a simplified network that preserves the essential functional and spatial structure of the original brain network while enabling computationally tractable analysis.

Figure 3.1 illustrates this process. The left panel shows the original graph, where each GROI is represented as an individual node and each WROI is represented a the regions in the middle of the GROIs. Based on their spatial coordinates, GROIs are grouped into communities, each consisting of two GROIs in this example. In the transformed version (middle panel), spatially proximate GROIs are aggregated into these communities. As a result, the streams between nodes that are now part of the same community become redundant. In the final graph (right panel), aggregated GROI communities function as consolidated GROIs. Importantly, WROIs and hence tumorous regions preserve their original structure, ensuring that the tumor's anatomical boundaries remain unchanged while significantly reducing the computational complexity of the problem.

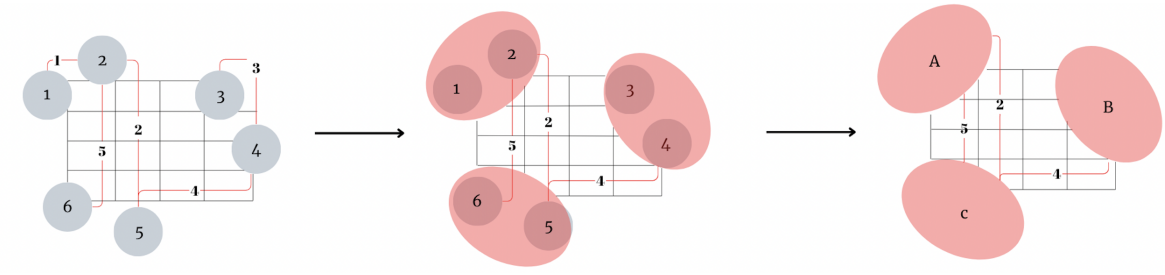

Figure 3.1: Schematic illustration of the aggregation heuristic approach. Grey nodes indicate GROIs, and the central square structure corresponds to WROIs.

The aggregated graph is solved using the optimization model described in Section 2. The resection plan obtained from the aggregation heuristic is mapped back to the original network. As formalized in Algorithm 1, global efficiency

(GE) is computed on the original graph to evaluate the solution's quality. This approach preserves the original network's topological features while achieving computational tractability - particularly beneficial for large-scale instances.

Tables 3.1 and 3.2 present the list of stream connections before and after the aggregation heuristic. Initially, the graph contains five streams connecting individual GROIs. For instance, stream-1 connects GROIs 1 and 2. After aggregation, since both GROIs 1 and 2 are merged into the same aggregated GROI (A), this stream becomes redundant. In contrast, stream-2 initially connects GROIs 2 and 5. After aggregation, GROI 2 becomes part of group A and GROI 5 becomes part of group C, so in the final graph, stream-2 now connects aggregated GROIs A and C.

Stream ID	**Start GROI**	**End GROI**
1	1	2
2	2	5
3	3	4
4	4	5
5	2	6

Table 3.1: List of streams and their corresponding start and end GROIs in the original graph

Stream ID	**Start GROI**	**End GROI**
1	A	A
2	A	C
3	B	B
4	B	C
5	A	C

Table 3.2: List of streams and their corresponding start and end GROIs in the aggregated graph

Tables 3.3 and 3.4 provide matrices that show the number of connections between the GROIs in the initial and final graphs, respectively. These matrices clearly reflect how the connections between nodes are transformed by the aggregation. For example, the stream between node pairs $(2, 5)$ and $(2, 6)$ in the original graph are now represented as streams between A and C in the final structure, reflecting the change in community assignments.

	1	2	3	4	5	6
1	0	1	0	0	0	0
2	1	0	0	0	1	1
3	0	0	0	1	0	0
4	0	0	1	0	1	0
5	0	1	0	1	0	0
6	0	1	0	0	0	0

Table 3.3: Number of streams of the original graph

	A	B	C
A	1	0	2
B	0	1	1
C	2	1	0

Table 3.4: Number of streams of the aggregated graph

In order to aggregate GROIs, we used the greedy_modularity_communities function from Python's NetworkX package [50]. This aggregation approach successfully reduced our GROI count from 379 to 190 while preserving critical network properties and reduced the number of hitting sets in the model by half. All subsequent analyses in this thesis utilize this aggregation framework, ensuring computational tractability without compromising the anatomical fidelity of tumor boundaries or the evaluation of global efficiency on the original network.

Chapter 4

Computational Experiments

In this chapter, we examine the effectiveness of our modeling and solution approach through a series of experiments. We focus on evaluating the performance of the aggregation heuristic, analyzing how tumor location and size affect the outcomes, and comparing our model's performance on real tumor instances with a worst-case resection baseline.

We use anatomical data from the HCP-MMP Atlas [17] to represent the healthy brain network. The atlas provides a parcellation of the cortex into 379 GROIs, along with tractography data containing approximately one million white matter axonal fibers. Using the 3D spatial coordinates of the GROIs, we construct their spatial connectivity by identifying neighboring regions. For the white matter, we rely on diffusion tensor imaging (DTI)-based tractography [13] to capture the full set of streamlines. Each streamline is mapped by its start and end points, and we identify all WROIs that the streamline passes through. This allows us to associate each streamline with a set of WROIs it traverses. Finally, we use the spatial coordinates of the WROIs to build their spatial connectivity network, forming the basis for modeling both gray and white matter structure in our resection framework.

However, this dataset does not include any tumorous regions. Therefore, we

synthetically generate tumors to simulate their presence. After creating the tumors, we also model their disruptive effect on the surrounding healthy regions to reflect the impact of real tumor growth. This section presents the results of these experiments and evaluates the performance of our approach under different conditions.

4.1 Experimental Setup

4.1.1 Tumor Generation

We begin by synthetically generating tumors that vary in both location and size. After selecting an initial region of interest, we expand the tumor outward in a spatially contiguous manner.

Creating a Tumor Instance:

The tumor $\mathcal{T}$ is initialized with a randomly selected WROI n_0. New WROIs are iteratively added to $\mathcal{T}$ until the desired tumor volume is reached, with spatial contiguity enforced at each step. This ensures the tumor grows in a physically plausible manner. The process shown in Algorithm 2.

Algorithm 2 Initialize Tumorous Region

1: Initialize $\mathcal{T} \leftarrow \{n_0\}$, where n_0 is a randomly selected starting WROI
2: **while** the volume of the tumorous region is below the desired volume value **do**
3: Randomly select a new WROI from the set of neighboring WROIs of the current tumorous WROIs and expand $\mathcal{T}$
4: **end while**

Once the tumor location (i.e. tumorous WROIs) is fixed, we model the tumor density in the selected volume.

Core and Periphery Definition:

A tumor consists of two distinct regions: a core, where the tumor concentration

is at its highest, and a periphery that surrounds the core where the tumor concentration gradually decreases. Figure 4.1 illustrates this structure on a brain network image. The red area represents the tumorous region. In this tumorous region, there is dark and light regions, the darker region represents the tumor core and the lighter region represents the tumor periphery. This structure mimics real tumor growth patterns, where cellular density is typically greatest at the center.

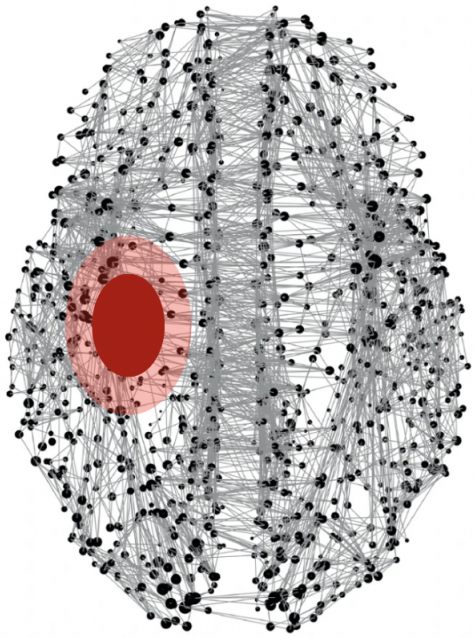

Figure 4.1: Visualization of tumor density, the darker regions represent the tumor core, lighter regions represent the tumor periphery on a brain network illustration [2].

When the tumor reaches its final volume, we determine the core and periphery regions through the following process. First, we calculate the tumor's center point by taking the mean spatial coordinates of all ROIs in the tumorous region. This gives us the geometric center of the tumor mass.

Using these center coordinates, we then compute the distance from the center to the farthest ROI in the tumor. This maximum distance helps define the tumor's overall spatial extent. We then apply pre-determined fractions of this maximum distance to establish the core and periphery radii - for instance, we might define the core radius as 40% of the maximum distance, with the periphery extending

to 80%.

All ROIs that fall within the sphere centered at the tumor's center with the core radius are classified as part of the core region. These ROIs represent areas of maximum tumor density. The remaining tumorous ROIs that lie between the core radius and periphery radius are assigned to the periphery region, where tumor density shows a gradual decrease toward the edges.

Empirical Basis for Density Modeling

To guide our assumptions on how tumor density changes spatially, we refer to preliminary findings from an ongoing study conducted at Hacettepe University by our clinical collaborators. Results of this study are obtained from real patient data. Figure 4.2 illustrates how tumor density decreases from the core toward the boundary of the tumor. The x-axis represents the normalized fraction of the distance from the tumor center to the boundary, and the y-axis shows the corresponding tumor density. As seen in the figure, the density is highest at the core and steadily decreases toward the periphery. These observations support the assumption of a gradual decline in tumor density with distance from the center.

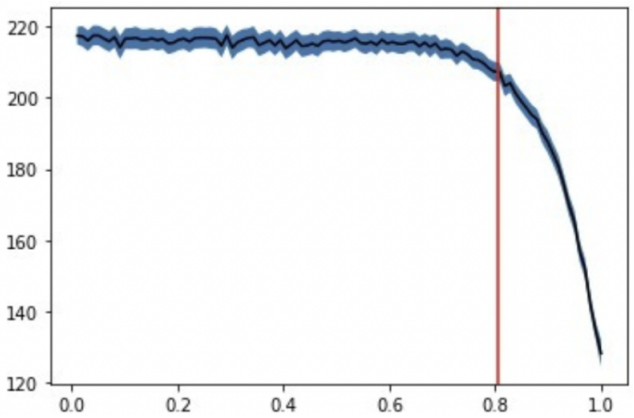

Figure 4.2: Tumor density profile based on real patient data. The x-axis represents the normalized distance from the tumor center, and the y-axis represents the corresponding tumor density.

Calculation of Tumor Density

Based on these observations, we model tumor density as a continuous function of distance from the tumor center. The density at a given point is calculated using the following formula:

$$\text{Density} = 1 - \frac{\max(\text{distance} - \text{core-radius}, 0)}{\text{periphery-radius}}$$

This formula computes the difference between 1 and a fraction where the numerator represents the distance beyond the core radius (capped at zero to ensure non-negative values) and the denominator corresponds to the periphery radius. By subtracting this fraction from 1, the function quantifies how tumor density reduces when moving away from the core toward the periphery. The resulting density value ranges from 0 to 1, with 0 indicating no tumor presence and 1 representing maximum tumor density. As the distance from the tumor center increases, the density gradually decreases, reflecting the transition from the dense core to the sparse periphery. This calculation provides insights into the spatial distribution of tumor cells within the tissue.

4.1.2 Tumor Disruption Simulation - Optimal Stream Removal

To simulate tumor-induced network disruption, we propose a method where streams passing through tumorous regions are removed based on the region's density, with higher density leading to more stream removal. This approach mimics real tumor disruption through two primary mechanisms: first, by severing critical connections between GROIs, and second, by directly reducing the network's global efficiency (GE). The density-dependent removal accurately reflects how actual tumors progressively impair brain connectivity, where regions with higher tumor cell concentration cause more severe disconnection of neural pathways while simultaneously degrading overall network efficiency.

Since streams often pass through multiple WROIs, each with distinct tumor densities, applying independent density-based removal criteria to individual WROIs can create conflicting requirements. The fundamental issue arises when

a single stream traverses WROIs with different density values - removal decisions appropriate for one region may be incompatible with another's tumor infiltration level.

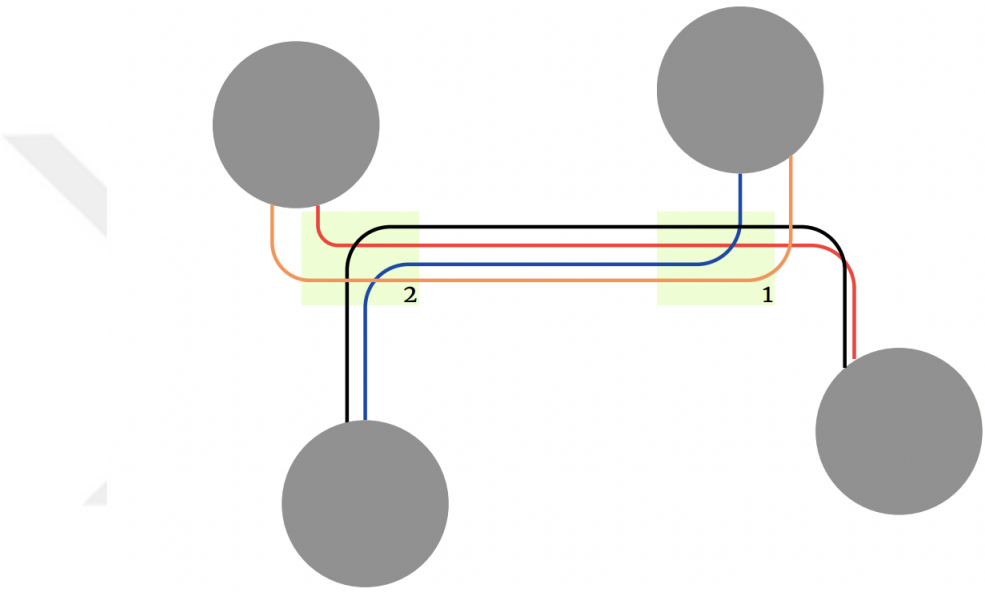

Figure 4.3: Visualization of stream pathways and regional overlap in edge resection modeling

This conflict is visually demonstrated in Figure 4.3. Consider the blue edge intersecting both WROI1 (tumor density = 0.75) and WROI2 (tumor density = 0.5). Following WROI1's higher density would require removing 3 streams, but this same removal would be disproportionately aggressive for WROI2, where the lower density suggests more conservative stream preservation. This creates a clinical-mathematical dilemma: satisfying one region's density requirement violates another's, potentially leading to either excessive or insufficient network disruption.

To resolve this conflict, we developed an optimization model where the preservation ratio for each WROI – defined as $\frac{\text{number of remaining streams through the WROI}}{\text{original number of streams through the WROI}}$ – varies proportionally with the WROI's distance from the tumor core. This proportionality ensures WROIs closer to the core (with higher density) undergo more

aggressive stream removal, while peripheral WROIs retain more connections. The model thus maintains biologically plausible disruption patterns that reflect decreasing tumor cell density with distance from the core.

Stream Disruption Optimization Model:
Parameters:

- $\mathcal{T}$ is the set of tumorous WROIs.
- ρ_i is the tumor density at tumorous WROI i, obtained from the density calculation, $i \in K$.
- a_{ji} is an indicator showing whether stream j passes through WROI i, $i \in K$, same as the previous models .
- $\mathcal{W}_i$ is the set of stream indices passing through WROI i, $i \in K$.

Decision Variable:

$$s_j = \begin{cases} 1, & \text{if the stream } j \text{ is removed} \quad j \in \mathcal{S} \\ 0, & \text{otherwise} \end{cases}$$

$$\begin{aligned} \text{Minimize} \quad & \sum_{j \in \mathcal{S}} s_j \\ \text{Subject to:} \quad & \sum_{j \in \mathcal{S}} a_{ji} \cdot s_j \geq \rho_i \cdot \sum_{j \in \mathcal{S}} a_{ji} \quad \forall i \in \mathcal{T} \\ & s_j = 0 \quad \text{if stream } j \notin \bigcup_{i \in \mathcal{T}} \mathcal{W}_i \\ & s_j \in \{0, 1\} \quad \forall j \end{aligned}$$

The objective minimizes the number of disrupted streams while ensuring that the fraction of removed connections in each tumorous ROI does not exceed the tumor density at that location. Streams that do not pass through any tumorous ROIs are fixed at zero (i.e., not removed).

Table 4.1 summarizes the results obtained from the model for 10 random synthetically generated tumor instances. The Tumor Volume, Core Volume, and Total WROI Volume columns represent the number of voxels corresponding to the tumorous regions, the tumor core, and the entire white matter, respectively. The Tumor% and Core% columns indicate the percentage of the white matter occupied by the tumor and its core. As seen in the table, the core tumor regions—which represent the highest-density areas—consistently exhibit 100% stream removal, confirming that these regions lost all its function for all instances. This completes the tumor instance generation process used in our study.

Instance	Core Streams	Tumorous Streams	Removed Streams	Removed Core Streams	Tumor Volume	Core Volume	Total WROI Volume	Tumor %	Core %
1	8,052	34,719	16,900	8,052	19,801	3,247	98,879	20.03%	3.28%
2	8,247	30,399	15,507	8,247	19,880	4,655	98,879	20.11%	4.71%
3	10,157	30,576	16,530	10,157	19,954	4,247	98,879	20.18%	4.30%
4	7,702	36,472	17,117	7,702	19,832	2,950	98,879	20.06%	2.98%
5	10,986	31,456	15,814	10,986	19,954	4,453	98,879	20.18%	4.50%
6	5,461	29,929	11,575	5,461	19,795	1,970	98,879	20.02%	1.99%
7	8,718	35,689	17,018	8,718	19,926	4,304	98,879	20.15%	4.35%
8	13,080	33,256	17,877	13,080	20,019	5,545	98,879	20.25%	5.61%
9	8,651	32,200	15,507	8,651	20,042	3,814	98,879	20.27%	3.86%
10	6,315	30,734	16,451	6,315	20,072	3,352	98,879	20.30%	3.39%

Table 4.1: Stream and Volume Statistics for Tumor Instances

4.2 Experimental Results

This section presents five computational analyses conducted on a structural brain network comprising 379 grey matter ROIs (GROIs) and 325 white matter ROIs (WROIs). The stream count varies dynamically across experiments due to scalability of the models used in experiments and tumor-induced disconnections (following Section 4.1's generation protocol). All models were implemented in Python 3.12.2 using NetworkX for graph operations and Gurobi 12.0 for optimization. Each analysis was repeated for 10 random instances per threshold level to ensure statistical robustness.

4.2.1 Performance Comparison of the Different Proposed Models

To compare the performance of the models introduced above, we ran all three models on the same set of problem instances. Specifically, we created 10 instances, each consisting of 379 GROIs, 325 WROIs, and 2000 edges, with varying tumor locations. Each of these instances was solved using all three model formulations. The optimization times for each model are presented in Figure 4.4.

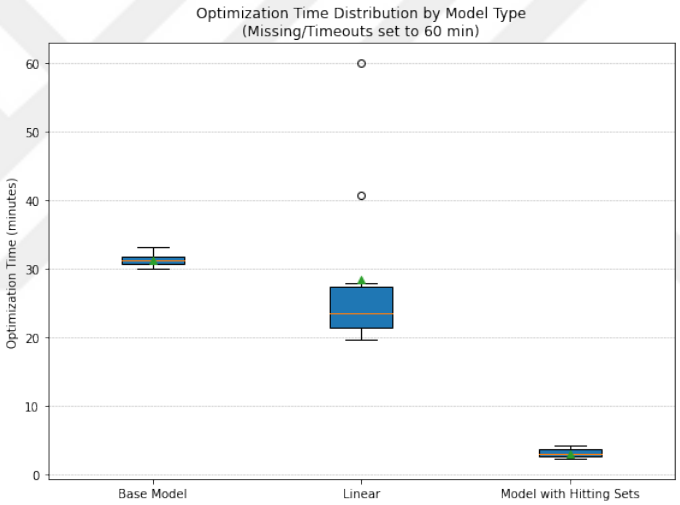

Figure 4.4: Optimization times of the different formulations

In general, the optimization times of the Base Model are higher than those of the Linear Model across most instances. However, this should not be interpreted as a consistent performance advantage for the Linear Model. For example, in one of the instances, the Linear Model takes more time to solve than the Base Model. Furthermore, in the another instance, the Linear Model was unable to complete the optimization due to a memory crash.

On the other hand, the model incorporating Hitting Sets significantly improves optimization times. It consistently solved all instances faster than the other two models. In addition to its superior performance in these smaller test cases, it is expected that the gap in optimization times will grow as instance size increases. The current instances were deliberately kept small to allow the Linear and Base

Models to complete without crashing. However, as problem scale increases, both of these models are likely to experience severe increases in optimization time—or may fail to solve altogether.

Given these observations, we chose to proceed with the Hitting Set Model for further analyses and experiments. It provides the best trade-off between modeling detail and computational efficiency, making it more scalable and robust for larger problem sizes. All resulting optimization times can be found in the Appendix C.1.

4.2.2 Efficiency of Aggregation Heuristic

To evaluate the efficiency of the aggregation heuristic, we compared it against the original model across different threshold levels. The stream count for this analysis is 10,000 streams. For each threshold, we ran 10 instances, first using the original model to record computation time, tumorous regions, disruption created by the tumorous regions, and tumor density. These parameters were then used as inputs for the aggregation heuristic to ensure a consistent comparison.

The aggregation heuristic significantly reduced computation time by simplifying the network structure through grey matter aggregation. Despite this simplification, the heuristic produced results very close to the original model. Figure 4.5 shows the scatter plots of the final GE values for both methods for all thresholds (0.7–0.9). These results demonstrate that the aggregation heuristic serves as a practical alternative to the original model, delivering near-optimal solutions with substantially improved computational speed. While the original formulation guarantees mathematically optimal results, its prohibitive runtime limits clinical feasibility which is precisely why we developed this heuristic approach to simplify the network topology while preserving solution quality.

As evidenced in Figure 4.6, the aggregation heuristic achieves dramatic runtime reductions compared to the original model. For large-scale datasets or time-sensitive clinical scenarios, this trade-off is fully justified: the minor deviations

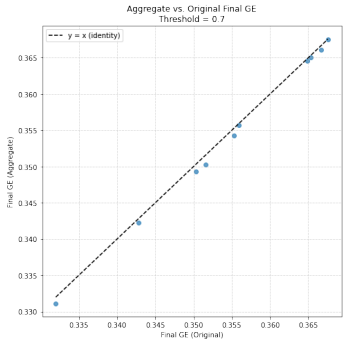

(a) Comparison of original model vs. aggregation heuristic at threshold = 0.7

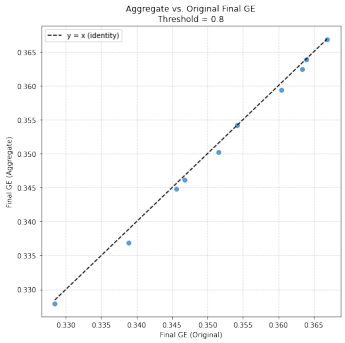

(b) Comparison of original model vs. aggregation heuristic at threshold = 0.8

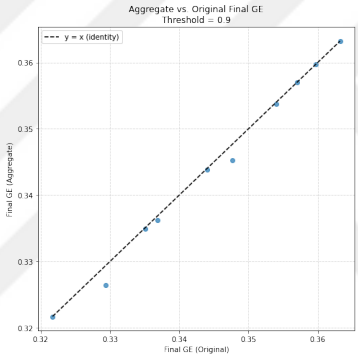

(c) Comparison of original model vs. aggregation heuristic at threshold = 0.9

Figure 4.5: Scatter plots comparing the original model and aggregation heuristic at different tumor volume resection thresholds

in global efficiency (GE) are clinically insignificant and are overwhelmingly outweighed by the orders-of-magnitude improvements in computational performance. All resulting for all instances, final GE values and total solution times can be found in the Appendix C.2.

4.2.3 Effect of Tumor Size on Resection

To systematically evaluate how tumor size impacts the resection process, we conducted experiments using three distinct tumor size categories: small (2% of total brain volume), medium (5%), and large (10%). For each tumor size class, we ran the aggregated model across 10 different instances at multiple threshold

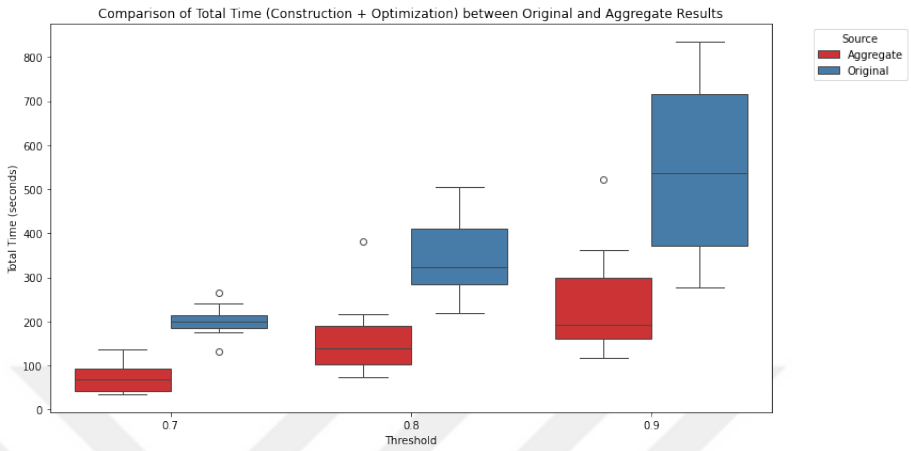

Figure 4.6: Comparison of total solving times of the Original vs Aggregated methods

levels with 100,000 streams. Means of global efficiency values for each instance are shown in the Figure 4.7a for all of the threshold values. The results were then normalized by dividing them by the graph's initial global efficiency and they are used to construct Figure 4.7b.

The threshold value of 0 represents the scenario where the model is not forced to remove any tumorous regions, meaning the Global Efficiency values at this threshold reflect only the disruption caused by the tumor's natural presence in the network. The results in Figure 4.7a clearly demonstrate that larger tumors cause significantly more disruption to the brain network compared to smaller tumors.

Specifically, Figure 4.7b show that the global efficiency values after the resection are lowest for large tumors, intermediate for medium tumors, and highest for small tumors. Also, decrease rate is increasing as the removal threshold increases. This pattern is expected because, at the same threshold percentage, larger tumors require removing substantially more tissue volume than smaller tumors, inevitably causing greater disruption to the network's connectivity.

The computational aspects show equally important trends. Smaller tumors consistently require less time to solve across all instances, while larger tumors demand progressively longer computation times. This performance difference stems

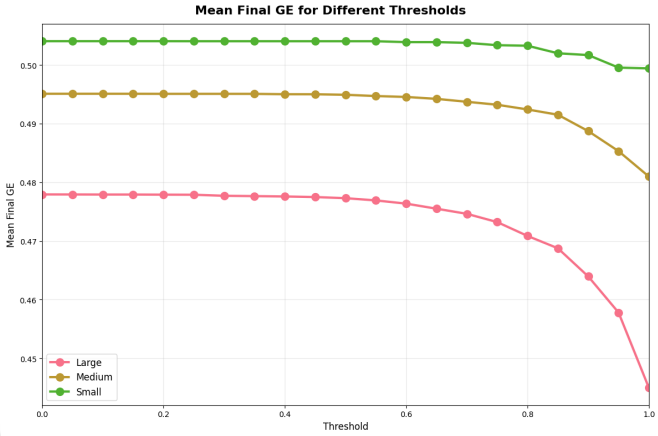

(a) Mean GE values

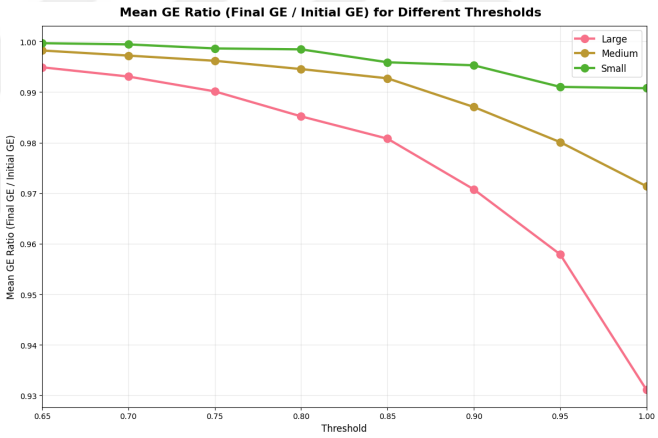

(b) Normalized Mean GE Values

Figure 4.7: Effect of Tumor Size on Model Outputs: Non-normalized Results Across All Thresholds (Top) and Normalized Results for Selected Thresholds (Bottom)

from the fundamental nature of the optimization problem: smaller tumors present a more constrained solution space with fewer possible resection configurations to evaluate, whereas larger tumors dramatically expand the number of potential solutions that must be considered. These timing results are visually confirmed in Figure 4.8, which captures the total computation time including both model construction and optimization phases for different tumor sizes. For all the instances, final GE values and total solution times for the Large,Small and Medium sized tumors and all threshold levels, can be found in the Appendix C.3.

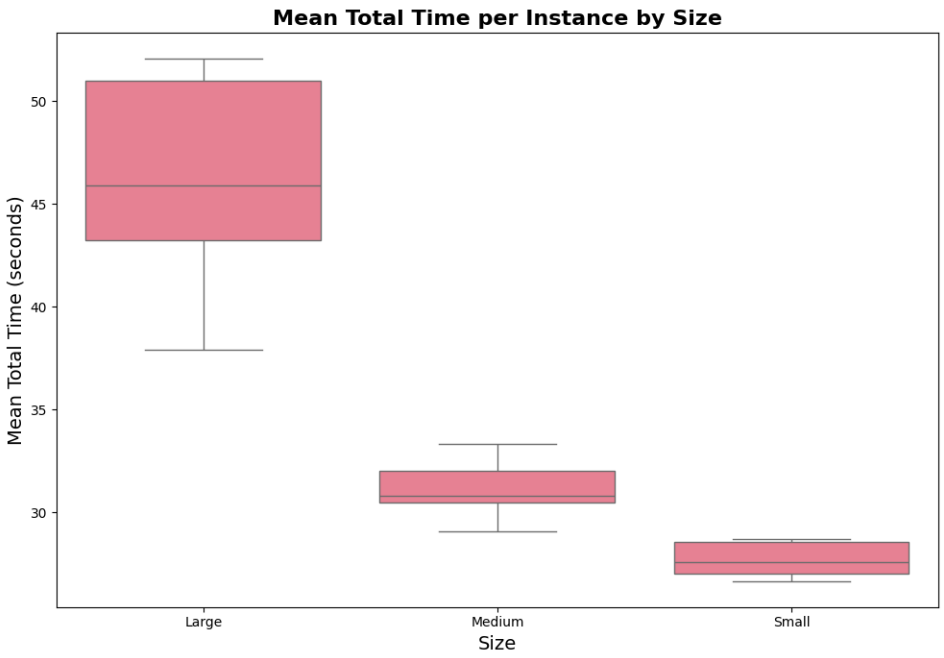

Figure 4.8: Mean optimization times for different tumor sizes

4.2.4 Effect of Tumor Location on Resection

To investigate how tumor location influences resection decisions, we conducted experiments on tumors situated in two distinct parts of the brain: the outer region—closer to the GROIs called shallow tumors, and the inner region—closer to the center of the brain called deep tumors. The center is calculated as the mean spatial coordinate of all WROIs. These experiments were performed on networks with 1 million edges and solved using the aggregation heuristic model.

We first generated a tumor located in the outer region of the brain and then gradually shifted it toward the center. This process was repeated for 10 different instances. An example of the generated tumors are illustrated in Figure 4.9, where the tumorous regions are marked in green. Figure 4.9a shows the shallow tumor, while Figure 4.9b displays the deep tumor. In both cases, the tumor volume is approximately 6% of the total white matter volume.

The corresponding resection outcomes are shown in red in Figure 4.10. In the shallow tumor instance, the Global Efficiency (GE) of the brain decreases

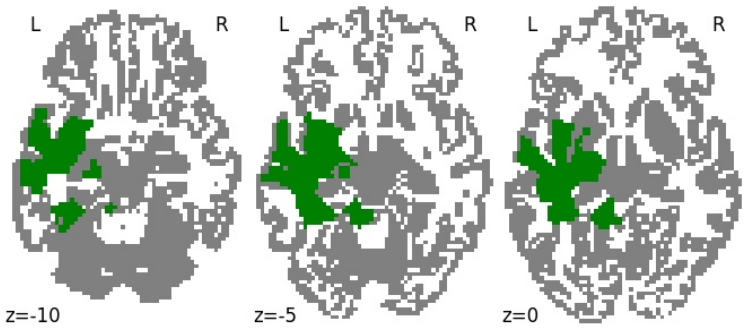

(a) Tumor located near cortical regions -shallow tumor

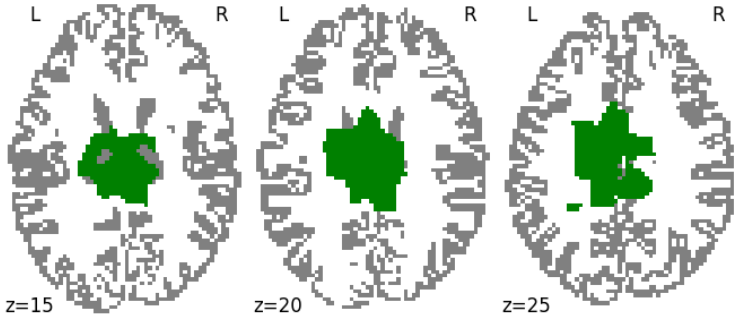

(b) Tumor located near central white matter - deep tumor

Figure 4.9: Comparison of Tumor Locations for Analyzing Resection Outcomes

by approximately 2.08%. In contrast, when the tumor is deep tumor, the GE drops by about 6.6%. Both results include the tumor induced reduction as well. This outcome aligns with expectations, as WROIs closer to the center tend to be traversed by longer-range streams that connect more distant GROIs. Therefore, resecting central WROIs disrupts a greater portion of the brain's connectivity, leading to a more substantial decline in GE. All resulting GE values for shallow and deep tumors at each instance are shown in Appendix C.4.

As mentioned earlier, this analysis was repeated for 10 different instances with the tumor volumes changes between %4 and %7 of the White matter. The changes in Global Efficiency observed across these experiments are shown in the Graphs 4.11. In the Graph 4.11a, the GE change caused by the tumorous regions on the brain network is illustrated. For all the instances, deep tumors resulted in

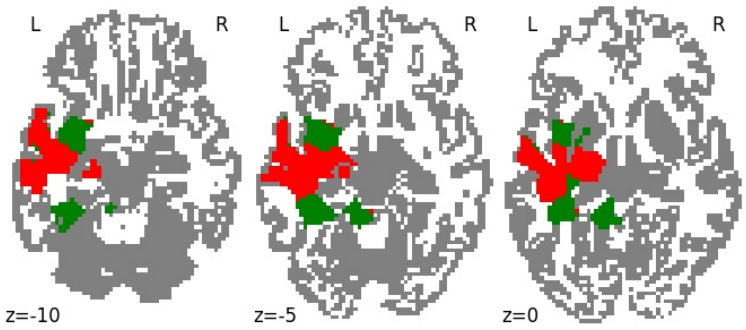

(a) Resulting resection for shallow tumor

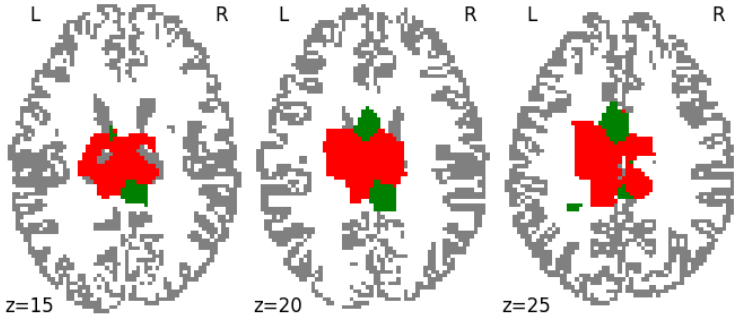

(b) Resulting resection for deep tumor

Figure 4.10: Effect of Tumor Location on Resection

grater GE reduction, even before the tumor resection. In the Graph 4.11b, GE decreases after the resection is shown. Deep tumors consistently result in greater reductions in GE compared to shallow tumors after the resection.

4.2.5 Real Tumor Instance Results

As our final analysis, we apply our model to a real tumor instance obtained from Hacettepe University Department of Neurosurgery. This tumor was manually segmented by our clinical collaborators from neuroimaging data using diffusion MRI and tractography pipelines and converted into a format compatible with our network model. The resulting dataset contains approximately 1 million streams

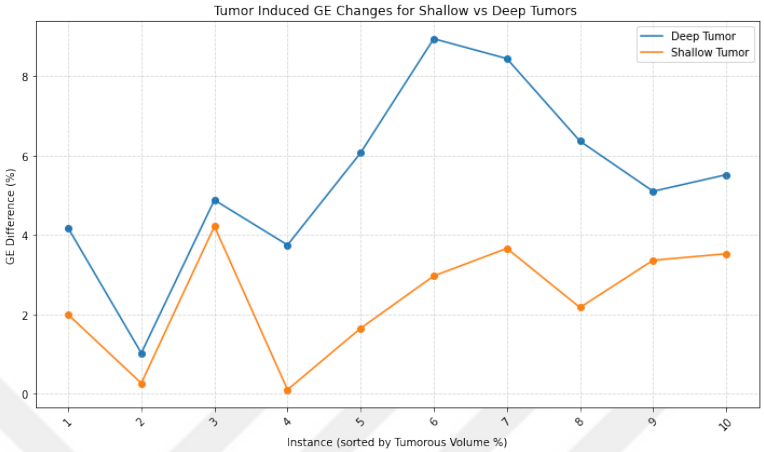

(a) Tumor Induced GE Change in Shallow vs Deep Tumors

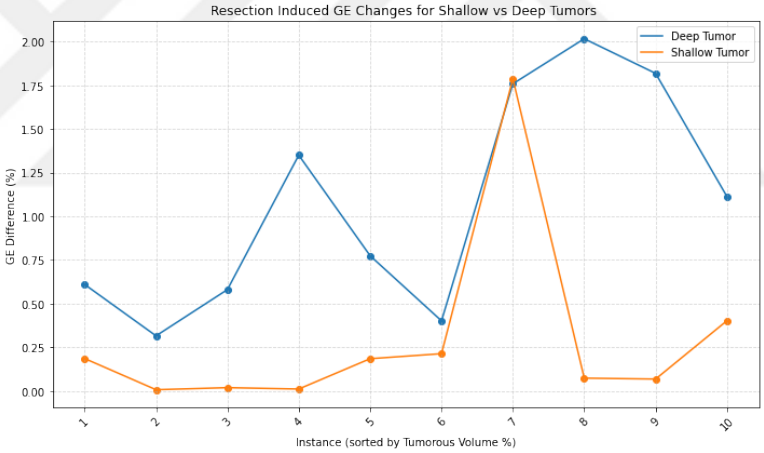

(b) Resection Induced GE Change in Shallow vs Deep Tumors

Figure 4.11: GE Changes Caused by Tumor-Induced and Resection Induced

connecting 379 GROIs and 278 WROIs.

This instance serves as a valuable test beyond synthetic cases, as it reflects the anatomical complexity, variability, and clinical realism of actual brain networks. The MRI-based tumor image is presented in Figure 4.12, while its digital representation within our Python-based framework is shown in Figure 4.13. One can note that these images are appear as mirror images of each other. This discrepancy arises due to differences in coordinate conventions between medical imaging software and our visualization framework. MRI scans are often stored in radiological convention, where the left side of the image corresponds to the

patient's right hemisphere. In contrast, our Python-based visualization adopts a neurological or matrix-based view, where the left side of the image corresponds to the left side of the matrix index. This convention mismatch leads to a mirrored appearance between the two representations, despite depicting the same anatomical structure.

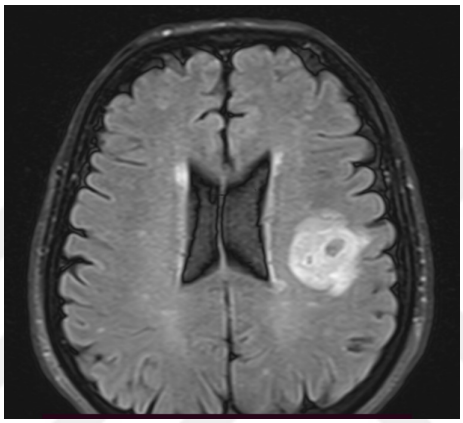

Figure 4.12: A real tumor instance observed using neuroimaging techniques

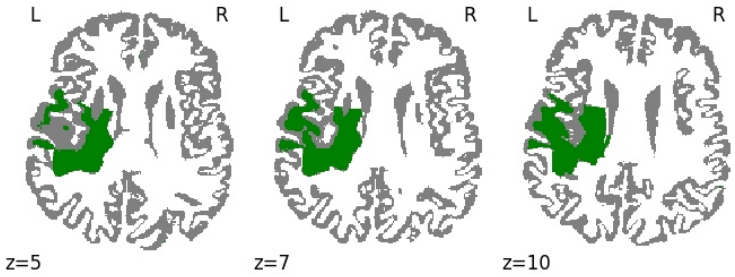

Figure 4.13: A real tumor instance illustrated using Python

To conduct this analysis, we used Base Nonlinear Model with Hitting Sets. In this section, it is named as the best-resection model and the worst resection model. The worst resection model serves as a comparison benchmark for our main resection model. Using this worst resection model, we evaluate real tumor instances to compare them against the best resection model results and demonstrate the potential functional damage of suboptimal surgical strategies.

The resected regions from both the best optimized and worst-case models are

illustrated in Figures 4.14a and 4.14b, respectively. One can clearly see that the removed regions differ significantly between the two approaches. Additionally, the resulting Global Efficiency (GE) values also vary: for the best resection model, final GE is 0.607, while for the worst-case resection, final GE drops to 0.594. These values were both computed at a threshold level of 0.8.

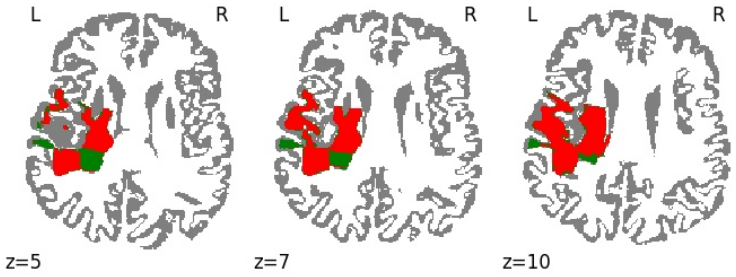

(a) A real tumor instance solved using our model and illustrated using Python

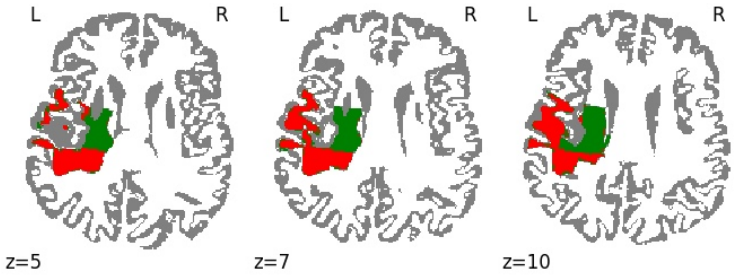

(b) A real tumor instance solved using our worst resection model and illustrated using Python

Figure 4.14: Real tumor analysis results

To further evaluate the performance across varying resection aggressiveness, we analyze the results of both models for multiple threshold values. Figure 4.15 illustrates these comparisons. For thresholds of 0 and 1—meaning that none or all of the tumorous regions are removed—the GE values are identical in both models, as expected. However, for all intermediate thresholds, our optimized model consistently preserves higher levels of GE. In the Table 4.2, all of the

initial and final GE results are shown. The initial GE in this table represents the GE after the tumor disruption on the brain graph.

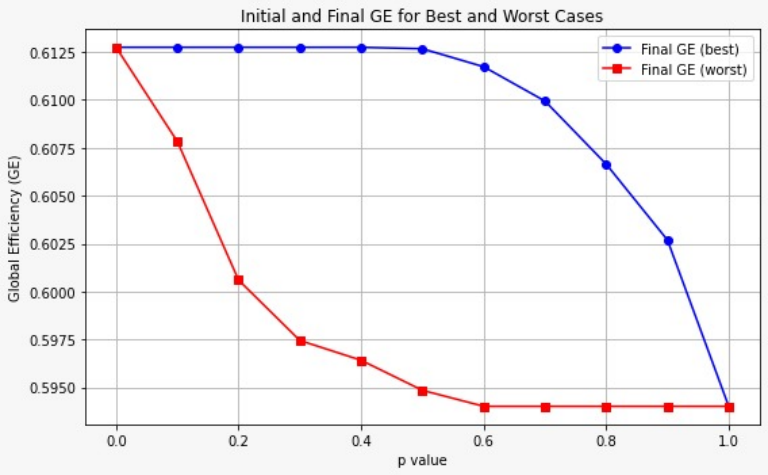

Figure 4.15: Best vs Worst Resection Models results for different threshold values

Table 4.2: Initial and Final GE Values for Best vs Worst Resection Models

p	Initial GE (best)	Initial GE (worst)	Final GE (best)	Final GE (worst)
0.0	0.612 747	0.612 747	0.612 747	0.612 747
0.1	0.612 747	0.612 747	0.612 747	0.607 832
0.2	0.612 747	0.612 747	0.612 747	0.600 595
0.3	0.612 747	0.612 747	0.612 747	0.597 447
0.4	0.612 747	0.612 747	0.612 747	0.596 413
0.5	0.612 747	0.612 747	0.612 672	0.594 846
0.6	0.612 747	0.612 747	0.611 732	0.594 012
0.7	0.612 747	0.612 747	0.609 943	0.594 012
0.8	0.612 747	0.612 747	0.606 651	0.594 012
0.9	0.612 747	0.612 747	0.602 689	0.594 012
1.0	0.612 747	0.612 747	0.594 012	0.594 012

Our models successfully solved this real instance within one hour, producing a feasible resection plan that satisfies all connectivity and spatial contiguity constraints. The "best" solution removed approximately 80% of the tumorous WROIs, while inducing only a 2.18% drop in GE. The model prioritized resecting the densest parts of the tumor while preserving WROIs responsible for long-range communication. On the other hand, the "worst" resection model resulted in 4.21% GE decrease, with the same level of tumorous WROI resection.

In quantitative terms, our model achieves a GE drop that is nearly half of what the worst-case scenario incurs, demonstrating its effectiveness in identifying functionally optimal resections.

From visual inspection, the resected region appears compact, biologically plausible, and localized to the tumor core. It avoids isolated or scattered removals and aligns with the spatial patterns typically observed in safe resection zones. These findings reinforce the model's practicality in handling real-world data and highlight its potential to inform surgical decision-making.

Unlike synthetic experiments, this real-case analysis demonstrates the model's clinical relevance and computational feasibility on large, high-fidelity networks. It sets the foundation for potential integration into preoperative workflows, where such a tool could support neurosurgeons in identifying risk-balanced resection regions.

Chapter 5

Conclusion and Future Work

In this research, we developed a mathematical optimization model for the brain tumor resection problem that accounts for both network connectivity and spatial constraints. We specifically focused on tumors that are primarily located within the white matter. To improve the efficiency of our model, we proposed different modeling techniques and introduced the aggregation heuristic, which enables solving larger-scale instances more effectively. For cases where real tumorous data was not available, we created synthetic tumor instances and modeled their disruptive effects on the brain network. We validated and then analyzed our model using both real and synthetic tumor data for different cases.

This work bridges the fields of neuroscience and operations research. It demonstrates how mathematical modeling and network analysis can be meaningfully applied to neuroscience and healthcare contexts. Beyond its academic contributions, this research provides neurosurgeons with a systematic and quantitative framework for planning brain tumor surgeries, aiming for maximum resection with minimal functional loss. It offers a reproducible computational approach that could be integrated into pre-surgical planning tools in the future.

As a direction for future work, we can extend the model to jointly consider the resection of both GROI and WROI regions. In real-life scenarios, brain

tumors may span both gray and white matter areas. Therefore, incorporating such cases into our modeling approach could lead to more comprehensive and realistic support for pre-surgical decision-making.

Bibliography

[1] D. Costarelli, M. Seracini, A. Travaglini, and G. Vinti, "Alzheimer biomarkers esteem by sampling kantorovich algorithm," *Mathematical Methods in the Applied Sciences*, vol. 46, p. 13506–13520, Apr. 2023.

[2] A. Avena-Koenigsberger, B. Misic, and O. Sporns, "Communication dynamics in complex brain networks," *Nature Reviews Neuroscience*, vol. 19, p. 17–33, Dec. 2017.

[3] P. D. Delgado-López, E. M. Corrales-García, J. Martino, E. Lastra-Aras, and M. T. Dueñas-Polo, "Diffuse low-grade glioma: a review on the new molecular classification, natural history and current management strategies," *Clinical and Translational Oncology*, vol. 19, p. 931–944, Mar. 2017.

[4] J. Pallud, *Diffuse Low-Grade Gliomas: What Does "Complete Resection" Mean?*, p. 153–161. Springer Netherlands, 2011.

[5] J. L. Keidel, S. R. Welbourne, and M. A. Lambon Ralph, "Solving the paradox of the equipotential and modular brain: A neurocomputational model of stroke vs. slow-growing glioma," *Neuropsychologia*, vol. 48, p. 1716–1724, May 2010.

[6] T. J. Brown, D. A. Bota, M. J. van Den Bent, P. D. Brown, E. Maher, D. Aregawi, L. M. Liau, J. C. Buckner, M. Weller, M. S. Berger, and M. Glantz, "Management of low-grade glioma: a systematic review and meta-analysis," *Neuro-Oncology Practice*, vol. 6, p. 249–258, Aug. 2018.

[7] P. Kumthekar, J. Raizer, and S. Singh, *Low-Grade Glioma*, p. 75–87. Springer International Publishing, Dec. 2014.

[8] N. B. Dadario and M. E. Sughrue, "Should neurosurgeons try to preserve non-traditional brain networks? a systematic review of the neuroscientific evidence," *Journal of Personalized Medicine*, vol. 12, p. 587, Apr. 2022.

[9] S.-P. Weathers, B. O'Brien, J. de Groot, C. A. Mahajan, and C. S. S. Prabhu, *Tumors of the Central Nervous System*. New York, NY: McGraw-Hill Medical, 2016.

[10] F. A. Azevedo, L. R. Carvalho, L. T. Grinberg, J. M. Farfel, R. E. Ferretti, R. E. Leite, W. J. Filho, R. Lent, and S. Herculano-Houzel, "Equal numbers of neuronal and nonneuronal cells make the human brain an isometrically scaled-up primate brain," *Journal of Comparative Neurology*, vol. 513, p. 532–541, Feb. 2009.

[11] M. Bear, B. Connors, and M. Paradiso, *Neuroscience: Exploring the Brain*. Wolters Kluwer, 2016.

[12] D. C. Van Essen, S. M. Smith, D. M. Barch, T. E. Behrens, E. Yacoub, and K. Ugurbil, "The wu-minn human connectome project: An overview," *NeuroImage*, vol. 80, p. 62–79, Oct. 2013.

[13] P. Basser, J. Mattiello, and D. LeBihan, "Mr diffusion tensor spectroscopy and imaging," *Biophysical Journal*, vol. 66, p. 259–267, Jan. 1994.

[14] M. F. Glasser, S. N. Sotiropoulos, J. A. Wilson, T. S. Coalson, B. Fischl, J. L. Andersson, J. Xu, S. Jbabdi, M. Webster, J. R. Polimeni, D. C. Van Essen, and M. Jenkinson, "The minimal preprocessing pipelines for the human connectome project," *NeuroImage*, vol. 80, p. 105–124, Oct. 2013.

[15] P. Hagmann, L. Cammoun, X. Gigandet, R. Meuli, C. J. Honey, V. J. Wedeen, and O. Sporns, "Mapping the structural core of human cerebral cortex," *PLoS biology*, vol. 6, no. 7, p. e159, 2008.

[16] E. Bullmore and O. Sporns, "Complex brain networks: graph theoretical analysis of structural and functional systems," *Nature Reviews Neuroscience*, vol. 10, p. 186–198, Feb. 2009.

[17] M. F. Glasser, T. S. Coalson, E. C. Robinson, C. D. Hacker, J. Harwell, E. Yacoub, K. Ugurbil, J. Andersson, C. F. Beckmann, M. Jenkinson, S. M. Smith, and D. C. Van Essen, "A multi-modal parcellation of human cerebral cortex," *Nature*, vol. 536, p. 171–178, July 2016.

[18] S. Arslan, S. I. Ktena, A. Makropoulos, E. C. Robinson, D. Rueckert, and S. Parisot, "Human brain mapping: A systematic comparison of parcellation methods for the human cerebral cortex," *NeuroImage*, vol. 170, p. 5–30, Apr. 2018.

[19] S. B. Eickhoff, B. Thirion, G. Varoquaux, and D. Bzdok, "Connectivity-based parcellation: Critique and implications," *Human Brain Mapping*, vol. 36, p. 4771–4792, Sept. 2015.

[20] E. Bullmore and O. Sporns, "The economy of brain network organization," *Nature Reviews Neuroscience*, vol. 13, p. 336–349, Apr. 2012.

[21] C.-Y. Lo, P.-N. Wang, K.-H. Chou, J. Wang, Y. He, and C.-P. Lin, "Diffusion tensor tractography reveals abnormal topological organization in structural cortical networks in alzheimer's disease," *The Journal of Neuroscience*, vol. 30, p. 16876–16885, Dec. 2010.

[22] V. Latora and M. Marchiori, "Efficient behavior of small-world networks," *Physical Review Letters*, vol. 87, Oct. 2001.

[23] S. M. Smith, "Overview of fmri analysis," *The British Journal of Radiology*, vol. 77, p. S167–S175, Dec. 2004.

[24] Y. Shahhosseini and M. F. Miranda, "Functional connectivity methods and their applications in fmri data," *Entropy*, vol. 24, p. 390, Mar. 2022.

[25] J. S. Elam, M. F. Glasser, M. P. Harms, S. N. Sotiropoulos, J. L. Andersson, G. C. Burgess, S. W. Curtiss, R. Oostenveld, L. J. Larson-Prior, J.-M. Schoffelen, M. R. Hodge, E. A. Cler, D. M. Marcus, D. M. Barch, E. Yacoub, S. M. Smith, K. Ugurbil, and D. C. Van Essen, "The human connectome project: A retrospective," *NeuroImage*, vol. 244, p. 118543, Dec. 2021.

[26] M. Rubinov and O. Sporns, "Complex network measures of brain connectivity: Uses and interpretations," *NeuroImage*, vol. 52, p. 1059–1069, Sept. 2010.

[27] T. Picart, A. Gautheron, C. Caredda, C. Ray, L. Mahieu-Williame, B. Montcel, and J. Guyotat, "Fluorescence-guided surgical techniques in adult diffuse low-grade gliomas: State-of-the-art and emerging techniques: A systematic review," *Cancers*, vol. 16, p. 2698, July 2024.

[28] L. Chen, J. Zhang, C. Chi, W. Che, G. Dong, J. Wang, Y. Du, R. Wang, Z. Zhu, J. Tian, N. Ji, X. Chen, and D. Li, "Lower-grade gliomas surgery guided by grpr-targeting pet/nir dual-modality image probe: a prospective and single-arm clinical trial," *Theranostics*, vol. 14, no. 2, p. 819–829, 2024.

[29] T. B. Belsuzarri, R. A. Sangenis, and J. M. Araujo, "Brain tumor surgery: supplemental intra-operative imaging techniques and future challenges," *Journal of Cancer Metastasis and Treatment*, vol. 0, no. 0, p. 0, 2015.

[30] H. Duffau, "A new concept of diffuse low-grade glioma surgery: Oncological and functional outcomes," *Neurology*, vol. 65, no. 6, pp. 1035–1038, 2005.

[31] S. L. Hervey-Jumper and M. S. Berger, "Advances in the surgical management of low-grade glioma: A review of indications, techniques, and outcomes," *Journal of Neuro-Oncology*, vol. 130, pp. 505–516, 2016.

[32] F. Henderson, K. G. Abdullah, R. Verma, and S. Brem, "Tractography and the connectome in neurosurgical treatment of gliomas: the premise, the progress, and the potential," *Neurosurgical Focus*, vol. 48, p. E6, Feb. 2020.

[33] G. Sparacia, G. Parla, V. Lo Re, R. Cannella, G. Mamone, V. Carollo, M. Midiri, and G. Grasso, "Resting-state functional connectome in patients with brain tumors before and after surgical resection," *World Neurosurgery*, vol. 141, p. e182–e194, Sept. 2020.

[34] Z. Chen, N. Ye, C. Teng, and X. Li, "Alternations and applications of the structural and functional connectome in gliomas: A mini-review," *Frontiers in Neuroscience*, vol. 16, Apr. 2022.

[35] Y. Wei, C. Li, Z. Cui, R. C. Mayrand, J. Zou, A. L. K. C. Wong, R. Sinha, T. Matys, C.-B. Schönlieb, and S. J. Price, "Structural connectome quantifies tumour invasion and predicts survival in glioblastoma patients," *Brain*, vol. 146, p. 1714–1727, Oct. 2022.

[36] H. A. Shah, L. Mittelman, S. Singha, R. Galvez, J. Cavallaro, B. Yaffe, G. Huang, J. W. Silverstein, and R. S. D'Amico, "Connectome imaging to facilitate preservation of the frontal aslant tract," *Clinical Neurology and Neurosurgery*, vol. 249, p. 108726, Feb. 2025.

[37] G. Herbet, H. Duffau, and E. Mandonnet, "Predictors of cognition after glioma surgery: connectotomy, structure-function phenotype, plasticity," *Brain*, vol. 147, p. 2621–2635, Apr. 2024.

[38] N. Samuel, A. Vetkas, A. Pancholi, C. Sarica, A. Loh, J. Germann, I. E. Harmsen, J. Tasserie, V. Milano, K. Yamamoto, S. K. Kalia, P. N. Kongkham, and A. M. Lozano, "A network-based approach to glioma surgery: Insights from functional neurosurgery," *Cancers*, vol. 13, p. 6127, Dec. 2021.

[39] A. Arulselvan, C. W. Commander, L. Elefteriadou, and P. M. Pardalos, "Detecting critical nodes in sparse graphs," *Computers amp; Operations Research*, vol. 36, p. 2193–2200, July 2009.

[40] M. Lalou, M. A. Tahraoui, and H. Kheddouci, "The critical node detection problem in networks: A survey," *Computer Science Review*, vol. 28, p. 92–117, May 2018.

[41] A. Veremyev, E. L. Pasiliao, and V. Boginski, "Measuring node criticality via closeness centrality in complex networks," *IEEE Transactions on Network Science and Engineering*, vol. 6, no. 3, pp. 440–453, 2019.

[42] A. Veremyev, O. A. Prokopyev, and E. L. Pasiliao, "Critical nodes for distance-based connectivity and related problems in graphs," *Networks*, vol. 66, p. 170–195, July 2015.

[43] V. Boginski and C. W. Commander, *Identifying Critical Nodes in Protein-Protein Interaction Networks*, p. 153–167. WORLD SCIENTIFIC, Feb. 2009.

[44] Y. Wang, A. Buchanan, and S. Butenko, "On imposing connectivity constraints in integer programs," *Mathematical Programming*, vol. 166, p. 241–271, Feb. 2017.

[45] R. Carvajal, M. Constantino, M. Goycoolea, J. P. Vielma, and A. Weintraub, "Imposing connectivity constraints in forest planning models," *Operations Research*, vol. 61, p. 824–836, Aug. 2013.

[46] A. Gainer-Dewar and P. Vera-Licona, "The minimal hitting set generation problem: Algorithms and computation," *SIAM Journal on Discrete Mathematics*, vol. 31, p. 63–100, Jan. 2017.

[47] A. Ignatiev, A. Morgado, and J. Marques-Silva, "PySAT: A Python toolkit for prototyping with SAT oracles," in *SAT*, pp. 428–437, 2018.

[48] A. Ignatiev, Z. L. Tan, and C. Karamanos, "Towards universally accessible SAT technology," in *SAT*, pp. 4:1–4:11, 2024.

[49] A. Clauset, M. E. J. Newman, and C. Moore, "Finding community structure in very large networks," *Physical Review E*, vol. 70, Dec. 2004.

[50] A. A. Hagberg, D. A. Schult, and P. J. Swart, "Exploring network structure, dynamics, and function using networkx," in *Proceedings of the 7th Python in Science Conference* (G. Varoquaux, T. Vaught, and J. Millman, eds.), (Pasadena, CA USA), pp. 11 – 15, 2008.

Appendix A

Base model with hitting sets and connectivity variables

This model addresses stream cuts and their impact on node connectivity through an alternative approach to the conventional z_s variable method. When a stream is cut, the connection between its corresponding nodes may be lost. While z_s variables were initially considered to accurately update the y_{ij} variables, they significantly increase the number of binary variables, leading to longer solution times. To improve computational efficiency, we instead employ hitting sets to determine lost connections. This approach maintains the model's accuracy in tracking connectivity changes while avoiding the computational overhead associated with z_s variables.

Objective Function

$$\text{Maximize} \quad \frac{1}{N \times (N-1)} \sum_{i \in \mathcal{N}} \sum_{j \in \mathcal{N}} \sum_{l=1}^{L} f(l) \left(u_{ij}^{l} - u_{ij}^{l-1} \right) \tag{A.1}$$

Constraints

$$\sum_{i \in \mathcal{T}} v_i x_i \geq v_0 \tag{A.2}$$

$$u_{ij}^{l} \leq \sum_{k=1}^{l-1} u_{ij}^{k} + \sum_{t \in \mathcal{N}, t \neq i, t \neq j} (1 - y_{ij}) g_{it} u_{tj}^{l-1}, \qquad \forall i, j \in \mathcal{N}, i \neq j, \forall l \in \{2, \ldots, L\} \tag{A.3}$$

$$u_{ij}^{1} \leq (1 - y_{ij}) g_{ij}, \qquad \forall i, j \in \mathcal{N}, i \neq j \tag{A.4}$$

$$1 - y_{ij} \leq |H_{ij}| - \sum_{i \in H} x_i \qquad \forall i, j \in \mathcal{N}, i \neq j, H_{ij} \in \mathcal{H}_{ij} \tag{A.5}$$

$$y_{ij} = 0 \qquad \forall i, j \in \mathcal{N}, (\mathrm{i,j}) \in E, b_{ij} = 1 \tag{A.6}$$

$$u_{ij}^{l} = u_{ji}^{l}, \qquad \forall i, j \in \mathcal{N}, \forall l \in \mathcal{L} \tag{A.7}$$

$$y_{ij} = y_{ji}, \qquad \forall i, j \in \mathcal{N} \tag{A.8}$$

$$u_{ii}^{0} = 1 \qquad \forall i \in \mathcal{N} \tag{A.9}$$

$$u_{ij}^{0} = 0 \qquad \forall i, j \in \mathcal{N}, i \neq j \tag{A.10}$$

$$\sum_{w \in S} x_w \geq x_u + x_v - 1, \qquad \forall S \in \Gamma(u, v), \quad \forall u, v \in \mathcal{K}, (u, v) \notin E \tag{A.11}$$

$$x_k \in \{0, 1\} \qquad \forall k \in \mathcal{K} \tag{A.12}$$

$$y_{ij} \in \{0, 1\} \qquad \forall i, j \in \mathcal{N} \tag{A.13}$$

$$u_{ij}^{l} \in \{0, 1\} \qquad \forall i, j \in \mathcal{N}, l \in \mathcal{L} \tag{A.14}$$

This model retains the global efficiency maximization objective (A.1), with constraints (A.5) introducing the hitting set mechanism to enforce connectivity loss when all nodes in a pair's hitting set are resected. All remaining constraints - including tumor volume thresholds (A.2), path length assignments (A.3) and (A.4), spatial connectivity preservation (A.11), and binary declarations (A.12-A.14) - are identical to the previous base line formulation.

Appendix B

Base model without connectivity variables

This model preserves most constraints from baseline formulation while implementing a key simplification: we eliminate the y_{ij} variables previously used to track node connectivity. Instead, connectivity is now determined directly through the u_{ij}^1 variables in the constraint set. This modification follows the same rationale as our earlier removal of z_s variables - to enhance computational efficiency without sacrificing model accuracy. By reducing the number of binary variables while maintaining equivalent functionality through u_{ij}^1, we achieve faster solution times while preserving all essential network connectivity information required for global efficiency optimization.

Objective Function

$$\text{Maximize} \quad \frac{1}{N \times (N-1)} \sum_{i \in \mathcal{N}} \sum_{j \in \mathcal{N}} \sum_{l=1}^{L} f(l) \left(u_{ij}^{l} - u_{ij}^{l-1} \right) \tag{B.1}$$

Constraints

$$\sum_{i \in \mathcal{T}} v_i x_i \geq v_0 \tag{B.2}$$

$$u_{ij}^k \leq \sum_{l=1}^{k-1} u_{ij}^l + \sum_{t \in \mathcal{N}, t \neq i, t \neq j} u_{it}^1 u_{tj}^{k-1}, \qquad \forall i, j \in \mathcal{N}, i \neq j, \forall k \in \{2, \ldots, L\} \tag{B.3}$$

$$u_{ij}^1 \leq \sum_{s \in S} e_{ij}^s (1 - z_s), \qquad \forall i, j \in \mathcal{N}, i \neq j \tag{B.4}$$

$$z_s \geq \frac{1}{K} \sum_{k \in \mathcal{K}} a_{sk} x_k, \qquad \forall s \in \mathcal{S} \tag{B.5}$$

$$u_{ij}^l = u_{ji}^l, \qquad \forall i, j \in \mathcal{N}, \forall l \in \mathcal{L} \tag{B.6}$$

$$\sum_{w \in S} x_w \geq x_u + x_v - 1, \qquad \forall S \in \Gamma(u, v), \quad \forall u, v \in \mathcal{K}, (u, v) \notin E \tag{B.7}$$

$$x_k \in \{0, 1\} \qquad \forall k \in \mathcal{K} \tag{B.8}$$

$$z_s \in \{0, 1\} \qquad \forall s \in \mathcal{S} \tag{B.9}$$

$$u_{ij}^l \in \{0, 1\} \qquad \forall i, j \in \mathcal{N}, l \in \mathcal{L} \tag{B.10}$$

The objective function (B.1) maintains the consistent goal of maximizing global efficiency through optimal resection planning. Constraint (B.2) ensures the resected tumor volume exceeds the specified threshold. For path length determination, (B.3) correctly sets the path length variables regardless of direct edge connections, mirroring the functionality of (2.11) from the first model. The model introduces (B.4) to enforce path consistency, specifically preventing length-1 paths between nodes when their connecting stream is cut. All other constraints retain their previous formulations from earlier models, maintaining continuity in handling spatial contiguity, binary variable declarations, and network connectivity rules.

Appendix C

Results

C.1 Computational times for the different models

Table C.1: Construction and Total Times for Different Models

Model	Instance	Constr Time	Total Time
Base Model	1	29.80	31.15
Base Model	2	30.03	31.62
Base Model	3	29.70	30.65
Base Model	4	29.93	30.30
Base Model	5	30.27	31.88
Base Model	6	29.73	29.97
Base Model	7	30.17	33.22
Base Model	8	30.20	30.65
Base Model	9	30.20	32.00
Base Model	10	30.18	31.40
Linear Model	1	17.80	22.00
Linear Model	2	17.77	21.33

(Continued on next page)

(Continued from previous page)

Model	Instance	Constr Time	Opt Time
Linear Model	3	17.80	20.32
Linear Model	4	18.05	40.77
Linear Model	5	18.05	25.05
Linear Model	6	17.92	19.67
Linear Model	7	60.00	60.00
Linear Model	8	17.25	21.55
Linear Model	9	17.48	27.92
Linear Model	10	17.73	26.12
Model with Hitting Sets	1	1.53	3.93
Model with Hitting Sets	2	1.57	3.15
Model with Hitting Sets	3	1.50	2.43
Model with Hitting Sets	4	1.63	2.80
Model with Hitting Sets	5	1.72	4.03
Model with Hitting Sets	6	1.48	2.58
Model with Hitting Sets	7	1.77	4.20
Model with Hitting Sets	8	1.68	2.30
Model with Hitting Sets	9	1.67	3.08
Model with Hitting Sets	10	1.70	2.87

C.2 Computational times (in seconds) and GE values for the aggregate and original methods

Table C.2: Comparison of Final GE and Total Time for Aggregate and Original models across instances and thresholds.

Instance	Threshold	Source	Final GE	Total Time (s)
1	0.7	Aggregate	0.3661	57
1	0.7	Original	0.3667	189
1	0.8	Aggregate	0.3625	153
1	0.8	Original	0.3634	282
1	0.9	Aggregate	0.3570	206
1	0.9	Original	0.3570	377
2	0.7	Aggregate	0.3650	34
2	0.7	Original	0.3653	132
2	0.8	Aggregate	0.3639	104
2	0.8	Original	0.3639	219
2	0.9	Aggregate	0.3597	139
2	0.9	Original	0.3597	278
3	0.7	Aggregate	0.3311	80
3	0.7	Original	0.3320	208
3	0.8	Aggregate	0.3280	125
3	0.8	Original	0.3285	413
3	0.9	Aggregate	0.3217	155
3	0.9	Original	0.3217	603
4	0.7	Aggregate	0.3557	35
4	0.7	Original	0.3559	195
4	0.8	Aggregate	0.3542	73
4	0.8	Original	0.3541	288
4	0.9	Aggregate	0.3452	175
4	0.9	Original	0.3477	363

Instance	Threshold	Source	Final GE	Total Time (s)
5	0.7	Aggregate	0.3645	137
5	0.7	Original	0.3648	265
5	0.8	Aggregate	0.3594	381
5	0.8	Original	0.3604	504
5	0.9	Aggregate	0.3537	522
5	0.9	Original	0.3540	741
6	0.7	Aggregate	0.3676	39
6	0.7	Original	0.3676	176
6	0.8	Aggregate	0.3668	101
6	0.8	Original	0.3669	279
6	0.9	Aggregate	0.3633	177
6	0.9	Original	0.3632	370
7	0.7	Aggregate	0.3493	78
7	0.7	Original	0.3503	203
7	0.8	Aggregate	0.3448	194
7	0.8	Original	0.3456	406
7	0.9	Aggregate	0.3349	362
7	0.9	Original	0.3351	835
8	0.7	Aggregate	0.3423	96
8	0.7	Original	0.3428	216
8	0.8	Aggregate	0.3369	174
8	0.8	Original	0.3389	303
8	0.9	Aggregate	0.3265	283
8	0.9	Original	0.3293	472
9	0.7	Aggregate	0.3503	110
9	0.7	Original	0.3516	241
9	0.8	Aggregate	0.3461	216
9	0.8	Original	0.3468	345
9	0.9	Aggregate	0.3363	303
9	0.9	Original	0.3369	769
10	0.7	Aggregate	0.3543	52
10	0.7	Original	0.3553	184

Instance	Threshold	Source	Final GE	Total Time (s)
10	0.8	Aggregate	0.3502	80
10	0.8	Original	0.3515	435
10	0.9	Aggregate	0.3439	116
10	0.9	Original	0.3441	643

C.3 Final GE values and computational times for large, medium and small sized tumors

Inst.	Thresh.	GE (L)	GE (M)	GE (S)	Time (L)	Time (M)	Time (S)
1	0.00	0.4710	0.4868	0.4934	20	21	21
1	0.05	0.4710	0.4868	0.4934	21	22	22
1	0.10	0.4708	0.4868	0.4934	22	23	23
1	0.15	0.4708	0.4868	0.4934	23	24	23
1	0.20	0.4708	0.4868	0.4934	24	25	24
1	0.25	0.4708	0.4868	0.4934	25	26	25
1	0.30	0.4708	0.4868	0.4934	26	26	25
1	0.35	0.4708	0.4868	0.4934	27	27	26
1	0.40	0.4708	0.4868	0.4934	28	28	26
1	0.45	0.4708	0.4868	0.4934	29	29	27
1	0.50	0.4708	0.4864	0.4934	31	30	28
1	0.55	0.4708	0.4862	0.4934	33	31	28
1	0.60	0.4708	0.4861	0.4934	36	32	29
1	0.65	0.4708	0.4860	0.4934	39	34	29
1	0.70	0.4706	0.4859	0.4934	44	35	30
1	0.75	0.4705	0.4858	0.4934	49	36	31
1	0.80	0.4703	0.4852	0.4934	52	37	31
1	0.85	0.4695	0.4839	0.4934	59	39	32
1	0.90	0.4688	0.4826	0.4934	61	41	33
1	0.95	0.4628	0.4820	0.4930	72	42	33
1	1.00	0.4587	0.4779	0.4930	75	43	34

Table C.3 – Continued

Inst.	Thresh.	GE (L)	GE (M)	GE (S)	Time (L)	Time (M)	Time (S)
2	0.00	0.4741	0.4870	0.5033	22	22	22
2	0.05	0.4741	0.4870	0.5033	23	23	23
2	0.10	0.4741	0.4870	0.5033	25	23	23
2	0.15	0.4741	0.4870	0.5033	25	24	24
2	0.20	0.4740	0.4869	0.5033	27	25	25
2	0.25	0.4740	0.4869	0.5033	28	26	25
2	0.30	0.4740	0.4869	0.5033	29	27	26
2	0.35	0.4739	0.4869	0.5033	31	28	26
2	0.40	0.4739	0.4869	0.5033	33	28	27
2	0.45	0.4738	0.4869	0.5033	35	29	28
2	0.50	0.4738	0.4869	0.5033	37	30	29
2	0.55	0.4738	0.4869	0.5033	40	31	29
2	0.60	0.4738	0.4869	0.5033	43	32	30
2	0.65	0.4736	0.4869	0.5033	50	33	31
2	0.70	0.4735	0.4869	0.5033	56	34	31
2	0.75	0.4732	0.4868	0.5030	60	35	32
2	0.80	0.4721	0.4868	0.5030	69	36	33
2	0.85	0.4713	0.4863	0.5014	76	37	33
2	0.90	0.4693	0.4829	0.5014	80	38	34
2	0.95	0.4640	0.4809	0.4975	88	39	35
2	1.00	0.4535	0.4772	0.4975	91	40	35
3	0.00	0.4719	0.4948	0.5010	21	20	20
3	0.05	0.4719	0.4948	0.5010	22	21	21
3	0.10	0.4719	0.4948	0.5010	24	22	22
3	0.15	0.4719	0.4948	0.5010	25	23	22
3	0.20	0.4719	0.4948	0.5010	27	24	23
3	0.25	0.4717	0.4948	0.5010	29	24	24
3	0.30	0.4700	0.4948	0.5010	33	25	24
3	0.35	0.4697	0.4948	0.5010	36	26	25
3	0.40	0.4696	0.4942	0.5010	40	27	26
3	0.45	0.4690	0.4942	0.5010	46	29	26
3	0.50	0.4685	0.4938	0.5010	53	30	27

Table C.3 – Continued

Inst.	Thresh.	GE (L)	GE (M)	GE (S)	Time (L)	Time (M)	Time (S)
3	0.55	0.4667	0.4938	0.5010	60	31	28
3	0.60	0.4656	0.4938	0.5010	72	32	28
3	0.65	0.4645	0.4935	0.5010	81	33	29
3	0.70	0.4626	0.4934	0.5010	94	35	29
3	0.75	0.4622	0.4923	0.5006	103	37	30
3	0.80	0.4599	0.4922	0.5006	114	38	31
3	0.85	0.4547	0.4914	0.4987	134	39	32
3	0.90	0.4498	0.4876	0.4974	159	41	32
3	0.95	0.4442	0.4865	0.4955	169	42	33
3	1.00	0.4371	0.4792	0.4955	172	43	34
4	0.00	0.4793	0.4848	0.4939	23	22	21
4	0.05	0.4793	0.4848	0.4939	25	23	22
4	0.10	0.4793	0.4848	0.4939	27	24	23
4	0.15	0.4793	0.4848	0.4939	29	24	24
4	0.20	0.4793	0.4848	0.4939	31	25	24
4	0.25	0.4793	0.4848	0.4939	33	26	25
4	0.30	0.4793	0.4848	0.4939	34	27	26
4	0.35	0.4793	0.4848	0.4939	36	28	26
4	0.40	0.4793	0.4848	0.4939	38	29	27
4	0.45	0.4791	0.4848	0.4939	41	30	28
4	0.50	0.4786	0.4848	0.4939	45	30	28
4	0.55	0.4781	0.4834	0.4939	47	32	29
4	0.60	0.4754	0.4828	0.4939	53	34	30
4	0.65	0.4739	0.4821	0.4939	61	36	31
4	0.70	0.4720	0.4803	0.4939	64	38	31
4	0.75	0.4672	0.4782	0.4926	71	40	32
4	0.80	0.4606	0.4758	0.4926	111	42	33
4	0.85	0.4560	0.4741	0.4926	165	44	33
4	0.90	0.4449	0.4688	0.4919	273	45	34
4	0.95	0.4417	0.4603	0.4899	294	47	35
4	1.00	0.4332	0.4573	0.4892	298	48	36

Table C.3 – Continued

Inst.	Thresh.	GE (L)	GE (M)	GE (S)	Time (L)	Time (M)	Time (S)
5	0.00	0.4825	0.5051	0.5102	22	23	22
5	0.05	0.4825	0.5051	0.5102	23	24	22
5	0.10	0.4825	0.5051	0.5102	25	25	23
5	0.15	0.4825	0.5051	0.5102	26	26	24
5	0.20	0.4825	0.5051	0.5102	26	27	24
5	0.25	0.4825	0.5051	0.5102	27	28	25
5	0.30	0.4825	0.5051	0.5102	29	29	26
5	0.35	0.4825	0.5051	0.5102	30	30	27
5	0.40	0.4825	0.5051	0.5102	32	31	27
5	0.45	0.4825	0.5051	0.5102	34	32	28
5	0.50	0.4825	0.5051	0.5102	35	32	29
5	0.55	0.4825	0.5050	0.5102	37	33	29
5	0.60	0.4825	0.5050	0.5102	39	34	30
5	0.65	0.4823	0.5046	0.5102	43	36	31
5	0.70	0.4822	0.5041	0.5091	46	37	31
5	0.75	0.4818	0.5039	0.5091	49	39	32
5	0.80	0.4813	0.5037	0.5091	52	40	33
5	0.85	0.4796	0.5031	0.5061	59	42	34
5	0.90	0.4768	0.5007	0.5060	68	43	35
5	0.95	0.4689	0.4980	0.5060	75	44	35
5	1.00	0.4564	0.4847	0.5054	78	45	36
6	0.00	0.4644	0.4862	0.4983	20	20	20
6	0.05	0.4644	0.4862	0.4983	21	21	21
6	0.10	0.4644	0.4862	0.4983	23	22	21
6	0.15	0.4644	0.4862	0.4983	25	23	22
6	0.20	0.4644	0.4862	0.4983	26	24	23
6	0.25	0.4644	0.4862	0.4983	28	25	23
6	0.30	0.4644	0.4862	0.4983	30	26	24
6	0.35	0.4644	0.4861	0.4983	32	27	24
6	0.40	0.4644	0.4861	0.4983	33	28	25
6	0.45	0.4643	0.4861	0.4983	35	29	26
6	0.50	0.4643	0.4861	0.4983	37	30	26

Table C.3 – Continued

Inst.	Thresh.	GE (L)	GE (M)	GE (S)	Time (L)	Time (M)	Time (S)
6	0.55	0.4638	0.4861	0.4983	39	31	27
6	0.60	0.4635	0.4859	0.4968	41	32	28
6	0.65	0.4632	0.4848	0.4968	44	34	29
6	0.70	0.4622	0.4836	0.4968	50	35	29
6	0.75	0.4609	0.4838	0.4968	54	36	30
6	0.80	0.4588	0.4809	0.4968	62	38	31
6	0.85	0.4560	0.4795	0.4927	67	39	32
6	0.90	0.4512	0.4739	0.4926	74	41	32
6	0.95	0.4473	0.4656	0.4840	78	42	33
6	1.00	0.4288	0.4627	0.4840	81	43	34
7	0.00	0.4839	0.4986	0.5109	21	20	21
7	0.05	0.4839	0.4986	0.5109	22	21	22
7	0.10	0.4839	0.4986	0.5109	24	22	22
7	0.15	0.4839	0.4986	0.5109	25	22	23
7	0.20	0.4839	0.4986	0.5109	27	23	24
7	0.25	0.4839	0.4986	0.5109	29	24	24
7	0.30	0.4839	0.4986	0.5109	30	25	25
7	0.35	0.4839	0.4986	0.5109	32	26	25
7	0.40	0.4839	0.4986	0.5109	34	26	26
7	0.45	0.4839	0.4986	0.5109	35	27	26
7	0.50	0.4838	0.4985	0.5109	37	28	27
7	0.55	0.4836	0.4985	0.5109	41	29	28
7	0.60	0.4833	0.4983	0.5108	44	31	28
7	0.65	0.4800	0.4983	0.5108	47	32	29
7	0.70	0.4787	0.4982	0.5108	52	33	30
7	0.75	0.4768	0.4976	0.5105	57	34	30
7	0.80	0.4730	0.4970	0.5105	73	35	31
7	0.85	0.4711	0.4958	0.5105	80	36	32
7	0.90	0.4650	0.4945	0.5104	90	38	32
7	0.95	0.4592	0.4886	0.5102	101	39	33
7	1.00	0.4428	0.4869	0.5102	104	40	34

Table C.3 – Continued

Inst.	Thresh.	GE (L)	GE (M)	GE (S)	Time (L)	Time (M)	Time (S)
8	0.00	0.4872	0.5085	0.5120	23	23	22
8	0.05	0.4872	0.5085	0.5120	24	24	23
8	0.10	0.4872	0.5085	0.5120	25	25	23
8	0.15	0.4872	0.5085	0.5120	28	26	24
8	0.20	0.4871	0.5085	0.5120	29	27	25
8	0.25	0.4871	0.5085	0.5120	30	28	25
8	0.30	0.4871	0.5085	0.5120	31	29	26
8	0.35	0.4870	0.5085	0.5120	34	29	27
8	0.40	0.4871	0.5085	0.5120	36	30	27
8	0.45	0.4871	0.5085	0.5120	38	31	28
8	0.50	0.4871	0.5085	0.5120	40	32	29
8	0.55	0.4871	0.5085	0.5120	43	33	29
8	0.60	0.4871	0.5085	0.5120	45	34	30
8	0.65	0.4871	0.5085	0.5120	48	35	31
8	0.70	0.4871	0.5085	0.5120	51	36	31
8	0.75	0.4870	0.5085	0.5120	54	37	32
8	0.80	0.4870	0.5085	0.5120	58	38	33
8	0.85	0.4869	0.5082	0.5111	61	39	33
8	0.90	0.4848	0.5077	0.5111	68	40	34
8	0.95	0.4783	0.5055	0.5093	80	41	35
8	1.00	0.4637	0.5031	0.5093	83	42	36
9	0.00	0.4790	0.4908	0.5064	21	20	21
9	0.05	0.4790	0.4908	0.5064	23	21	22
9	0.10	0.4790	0.4908	0.5064	25	22	22
9	0.15	0.4790	0.4908	0.5064	27	23	23
9	0.20	0.4790	0.4908	0.5064	29	24	24
9	0.25	0.4790	0.4908	0.5064	30	24	24
9	0.30	0.4790	0.4908	0.5064	31	25	25
9	0.35	0.4790	0.4908	0.5064	33	26	25
9	0.40	0.4790	0.4908	0.5064	35	27	26
9	0.45	0.4789	0.4908	0.5064	36	28	27
9	0.50	0.4788	0.4908	0.5064	39	29	27

Table C.3 – Continued

Inst.	Thresh.	GE (L)	GE (M)	GE (S)	Time (L)	Time (M)	Time (S)
9	0.55	0.4783	0.4908	0.5064	41	30	28
9	0.60	0.4781	0.4908	0.5064	44	31	29
9	0.65	0.4771	0.4908	0.5064	48	31	29
9	0.70	0.4757	0.4906	0.5062	55	32	30
9	0.75	0.4729	0.4900	0.5045	69	34	31
9	0.80	0.4670	0.4892	0.5043	85	36	32
9	0.85	0.4665	0.4889	0.5030	95	37	32
9	0.90	0.4573	0.4856	0.5030	105	39	33
9	0.95	0.4492	0.4840	0.5013	109	40	34
9	1.00	0.4311	0.4812	0.5013	113	41	34
10	0.00	0.4860	0.5083	0.5111	20	21	21
10	0.05	0.4860	0.5083	0.5111	21	22	21
10	0.10	0.4860	0.5083	0.5111	22	23	22
10	0.15	0.4860	0.5083	0.5111	23	24	22
10	0.20	0.4860	0.5083	0.5111	24	25	23
10	0.25	0.4860	0.5083	0.5111	25	25	24
10	0.30	0.4860	0.5083	0.5111	27	26	24
10	0.35	0.4859	0.5083	0.5111	29	27	25
10	0.40	0.4854	0.5083	0.5111	31	28	26
10	0.45	0.4853	0.5083	0.5111	33	29	26
10	0.50	0.4848	0.5082	0.5111	36	30	27
10	0.55	0.4843	0.5077	0.5111	40	31	27
10	0.60	0.4836	0.5072	0.5111	45	32	28
10	0.65	0.4825	0.5066	0.5111	50	33	29
10	0.70	0.4816	0.5058	0.5111	58	34	29
10	0.75	0.4797	0.5052	0.5111	62	36	30
10	0.80	0.4786	0.5049	0.5103	66	38	31
10	0.85	0.4760	0.5040	0.5103	74	39	31
10	0.90	0.4715	0.5028	0.5096	84	40	32
10	0.95	0.4625	0.5016	0.5086	93	42	33
10	1.00	0.4442	0.4995	0.5086	96	43	33

C.4 Initial and Final GE values of shallow and deep tumors for all instances

Table C.4: Initial and final GE values for shallow and deep tumor types across instances.

Instance	Type	Initial GE Before Tumor Disruption	Initial GE After Tumor Disruption	Final GE After Tumor Resection
1	Deep	0.5916	0.5653	0.5539
1	Shallow	0.5916	0.5791	0.5787
2	Deep	0.5916	0.5659	0.5627
2	Shallow	0.5916	0.5667	0.5666
3	Shallow	0.5916	0.5808	0.5797
3	Deep	0.5916	0.5703	0.5668
4	Deep	0.5916	0.5652	0.5589
4	Shallow	0.5916	0.5730	0.5707
5	Deep	0.5916	0.5513	0.5416
5	Shallow	0.5916	0.5802	0.5699
6	Deep	0.5916	0.5873	0.5855
6	Shallow	0.5916	0.5900	0.5900
7	Deep	0.5916	0.5772	0.5694
7	Shallow	0.5916	0.5910	0.5909
8	Deep	0.5916	0.5718	0.5614
8	Shallow	0.5916	0.5720	0.5716
9	Deep	0.5916	0.5408	0.5386
9	Shallow	0.5916	0.5752	0.5740
10	Deep	0.5916	0.5600	0.5556
10	Shallow	0.5916	0.5828	0.5818